Review Article

Toward the multiscale nature of stress corrosion cracking

Xiaolong Liu [a, *], Woonggi Hwang [a], Jaewoong Park [a], Donghyun Van [b],
Yunlong Chang [c], Seung Hwan Lee [a], Sung-Yup Kim [d], Sangsoo Han [d],
Boyoung Lee [a]

[a] School of Aerospace and Mechanical Engineering, Korea Aerospace University, 76, Hanggongdaehang Road, Deogyang District, Goyang, Gyeonggi Province, 10540, Republic of Korea
[b] Daewoo Institute of Construction Technology, Republic of Korea
[c] School of Materials Science and Engineering, Shenyang University of Technology, PR China
[d] Computational Science Research Center, Korea Institute of Science and Technology, Republic of Korea

ARTICLE INFO

ABSTRACT

This article reviews the multiscale nature of stress corrosion cracking (SCC) observed by high-resolution characterizations in austenite stainless steels and Ni-base superalloys in light water reactors (including boiling water reactors, pressurized water reactors, and supercritical water reactors) with related opinions. A new statistical summary and comparison of observed degradation phenomena at different length scales is included. The intrinsic causes of this multiscale nature of SCC are discussed based on existing evidence and related opinions, ranging from materials theory to practical processing technologies. Questions of interest are then discussed to improve bottom-up understanding of the intrinsic causes. Last, a multiscale modeling and simulation methodology is proposed as a promising interdisciplinary solution to understand the intrinsic causes of the multiscale nature of SCC in light water reactors, based on a review of related supporting application evidence.
© 2018 Korean Nuclear Society, Published by Elsevier Korea LLC. This is an open access article under the CC BY-NC-ND license (http://creativecommons.org/licenses/by-nc-nd/4.0/).

1. Background

The stress corrosion cracking (SCC) of austenitic stainless steels or Ni-base alloys in light water reactors (LWRs) has been a cause of service failure and has consequently attracted continuous research efforts to determine the failure mechanisms involved. Investigations include a combination of autoclave acceleration tests, high-resolution characterization, theoretic analysis, and modeling and simulation.

In the conventional approach of integrated acceleration test—characterization—theory, typical works have systematically applied high-resolution characterization using focused ion beam—scanning electron microscope, analytical transmission electron microscopy, atom-probe tomography, secondary ion mass spectroscopy, 3-D tomography, micromechanical testing, and digital image correlation. These methods can provide multiscale (from the micrometer to the nanometer) understanding of the widely accepted SCC mechanisms such as the film-rupture model, hydrogen-related mechanisms, and the internal oxidation mechanism [1–3]. Aided by these state-of-the-art high-resolution characterization techniques, SCC in LWRs has been determined to include degradation phenomena at different length scales, involving surface or intergranular (IG) corrosion/oxidation, the fracture of oxides, grain boundary (GB) migration, elemental segregation, and dislocations sliding around the crack tip and on the crack flanks. Accordingly, research efforts have shifted from analyzing microstructural changes to analysis of the local chemistry and elasticity or plasticity of the crack-tip region [1,4]. However, in situ characterization (e.g., in situ transmission electron microscopy) is still highly restricted by the physical and chemical conditions of the autoclave acceleration tests, and consequently, the evidence obtained by characterization mainly reflects the final states of the local sites of interest, rather than the temporal and spatial evolution of the entire material failure process. As a result, a unified SCC mechanism that can account for all the multiscale nature of SCC is still needed to provide a more bottom-up understanding of their intrinsic causes.

At the same time, cutting-edge multiparadigms and multiscale modeling and simulation have helped to directly reveal multiscale physical or chemical failure processes. These include, for example, the relationship of the electron transfer behavior or the erratic motion of individual atoms at the Ångström scale to the rupturing of ionic bonds of the molecular template at nanoscale; to the deformation behavior of structural defects at mesoscale (between

Table 1
Operation conditions of light water reactors (LWRs).

LWRs type	Coolants type	Distinction between subcritical water and supercritical water	Inlet and outlet temperature (°C)	Operation pressure (MPa)	pH (room temperature)	References
Boiling water reactor (BWR)	Subcritical water	280°C < temperature <374 °C	280~288	7—8	6.1—8.1	[9]
Pressurized water reactor (PWR)		7 MPa < pressure <22.05 MPa	290~320	15—16	6.9—7.4	[10]
Supercritical water reactor (SCWR)	Supercritical water	Temperature > 374°C pressure >22.05 MPa	280~620	25	~7	[11,12]

nanoscale and microscale); and to the deformation and fracture behavior of the bulk at macroscale [5—8].

In light of this, the multiscale nature of SCC (mainly in the form of IG SCC) of austenitic stainless steels or Ni-base superalloys in the LWRs conditions, as classified in Table 1 [9—12], and in the context of existing opinions was reviewed and summarized. The potential intrinsic causes of the multiscale nature of SCC are discussed, while questions of interest are correspondingly raised regarding the potential mechanisms. Finally, multiparadigms and multiscale modeling and simulation are reviewed in terms of their related application to multiscale failure analysis and then a promising interdisciplinary solution is proposed for investigating the multiscale nature of SCC in the LWRs.

2. The multiscale nature of SCC

2.1. Surface corrosion and fracture of corrosion products

Although the chemical compositions of susceptible alloys are commonly modified to provide better anticorrosion performance, surface corrosion and the fracture of duplex corrosion products still frequently occur in materials exposed to high-temperature water and act as points of initiation of SCC failure, as illustrated in Figs. 1 and 2 [13,14]. Based on a review of surface corrosion and the fracture of corrosion products, some key common features that occur at different length scales are statistically summarized and are compared in Table 2 [2,13—35]. The results show the following:

(1) At nanoscale (in terms of thickness), the duplex corrosion products on the surfaces of the sampled austenitic alloys are composed of a rough and porous outer oxide layer and a continuous and dense inner oxide layer. The outer oxide layer features a mixture of sparse coarse-grained particles and fine-grained faced particles, whereas the inner oxide layer has uniformly fine grains.
(2) In the rough and porous outer oxide layer, nanoscale iron−nickel (Fe−Ni) or iron−chromium (Fe−Cr and Fe-rich)

M_3O_4 (M means Ni, Cr, Fe atoms) spinels were characterized as the major oxide phases for STS 304, STS 304L, STS 316, and STS 316L, whereas nanoscale Ni-rich spinels or (Fe-rich spinel and NiO) mixtures comprised the major oxide phases for Alloy 600, Alloy 625, Alloy 690, and Alloy 690 TT (thermally treated).

(3) In the continuous and dense inner oxide layer, nanoscale Cr−Fe (Cr-rich) M_3O_4 spinels were characterized as the major oxide phases for STS 304, STS 304L, STS 316, and STS 316L, whereas nanoscale [Cr_2O_3 and Cr−Ni (Cr-rich) M_3O_4 spinels] mixtures were the major oxide phases for Alloy 600, Alloy 625, Alloy 690, and Alloy 690 TT, along with penetrative CrO for Alloy 600 and Alloy 690 [36]. This inner oxide layer can initially act as a protective film for the matrix. As demonstrated, however, when there was not enough Cr from the GBs in Alloy 600 and Alloy 690 to replenish and repair the surface Cr_2O_3 or Cr-rich spinel layers during the successive rupture, this brittle film was fractured by the tensile strain [2,27,37]. Such brittle fracture of the continuous and dense inner oxide layer was also found in the STS 316 sample; a typical example is shown in Fig. 1 [14]. The role of tensile strain was specifically confirmed by finite element analysis [38].

2.2. IG corrosion and fracture of corrosion products

As a key transition stage from the initial surface corrosion to the initiation of SCC, IG corrosion and cracking contribute to the multiscale nature of SCC. A review of the changes in local chemistry and crack-tip elasticity or plasticity in this stage are summarized and compared in Table 3 [2,14,21,27,39—56]. The following were determined:

(1) At nanoscale (in terms of thickness), the duplex IG corrosion products in all of the sampled austenite alloys are composed of a continuous and dense inner oxide layer, penetrating double crack flanks, and discrete and porous
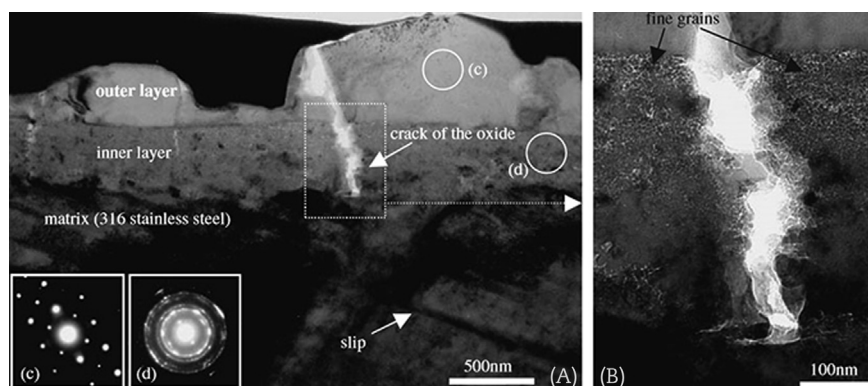

Fig. 1. The cross-sectional TEM of the nanoscale duplex surface oxides formed on STS 316 sample exposed to a PWR at 320°C for 500 h. (A) Cross-sectional morphology of duplex surface oxide film. (B) Enlargement of the crack within the film. (C) Diffraction pattern with spots from outer coarse-grained spinels. (D) Diffraction pattern with spots from inner fine-grained spinels [14] (Reprinted with permission from Taylor & Francis).
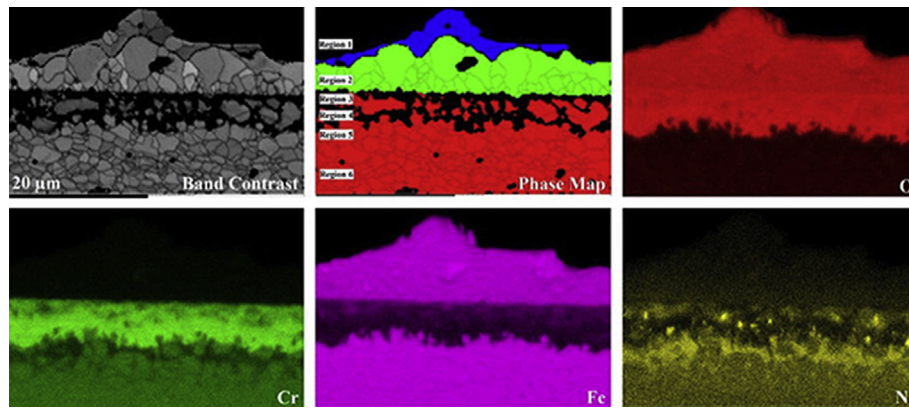PWR, pressurized water reactor; TEM, transmission electron microscopy.

Fig. 2. The mesoscale elements segregation of Cr, Fe, and Ni atoms by EDS within the duplex surface oxide film and the subsurface regions and phase map by EBSD occurred in thermomechanical−processed STS 316L sample exposed to a SCWR with 150 ppb dissolved O_2 at 600°C and 25 MPa for 1,000 h (red-austenite and spinels phases, green-magnetite phase, blue-hematite phase). (For interpretation of the references to color in this figure legend, the reader is referred to the Web version of this article.) [13] (Reprinted with permission from Elsevier).

EBSD, electron backscatter diffraction; EDS, energy dispersive X-ray spectroscopy; SCWR, supercritical water reactor.

Table 2
Statistical comparison in surface corrosion behavior of austenite alloys in simulated LWRs.

Base materials	Outer rough and porous oxide layer	Inner continuous and dense oxide layer	Test conditions	References
	Major oxide phases	Major oxide phases		
STS 304	$(Ni_{0.2}Fe_{0.8})(Fe_{0.95}Cr_{0.05})_2O_4$.	$(Ni_{0.2}Fe_{0.8})(Cr_{0.7}Fe_{0.3})_2O_4$.	PWR at 260°C for 1,000, 2,000, 5,000, 8,000, and 10,000 h.	[15]
	Fe-rich spinels.	Cr-rich spinels.	PWR at 360°C for 1,500 h.	[16]
	Fe_3O_4.	Fe−Cr spinels.	SCWR at 400°C, 450°C, 500°C, and 550°C.	[17]
STS 304L	$Fe(Cr/Ni)_2O_4$ spinels.	Cr-rich spinels.	PWR and SCWR at 340°C and 400°C for 500 h.	[18]
	Fe-rich oxides and Fe-Ni spinels.	Ni−Cr spinels.	SCWR at 450°C, 500°C, 550°C, and 600°C and 25 MPa for 1,680 h.	[19]
STS 316	Fe_3O_4.	Cr-rich spinels.	PWR at 320°C for 500 h.	[14]
	Fe_3O_4 and Fe_2O_3.	Cr_2O_3 and Fe-rich spinels.	SCWR at 350°C, 400°C, 450°C, and 500°C and 24 MPa for 250 h.	[20]
STS 316L	$Ni_{0.75}Fe_{2.25}O_4$.	$(Cr_2O_3+FeCr_2O_4)$ and Fe_3O_4.	PWR at 350°C for 2,000 h.	[21]
	Fe_3O_4.	Fe−Cr spinels.	SCWR from 400°C to 550°C.	[17]
	Fe_3O_4.	Cr_2O_3 and $FeCr_2O_4$ spinels.	SCWR at 600°C and 25 MPa for 100, 300, and 1,000 h.	[13]
Alloy 600	$(Ni_{0.9}Fe_{0.1})(Fe_{0.85}Cr_{0.15})_2O_4$.	$(Ni_{0.7}Fe_{0.3})(Fe_{0.3}Cr_{0.7})_2O_4$.	PWR at 260°C for 1,000, 2,000, 5,000, 8,000, and 10,000 h.	[22]
	Ni-Fe spinels.	Cr-rich spinels.	PWR at 320°C for 120 and 500 h.	[23]
	Ni-rich spinels.		PWR at 320°C for 1,000 h.	[24]
	NiO and Ni-Cr spinels.	Cr-rich oxides.	PWR at 325°C.	[25]
	$NiFe_2O_4$ and $Ni(Cr, Fe)_2O_4$.	$FeCr_2O_4$ spinels and Cr_2O_3.	PWR at 288°C and 338°C for 500, 1,000, 2,000, 3,000, 4,000, and 5,000 h.	[26]
	NiO.		SCWR at 360°C for 2,000 h, 390°C for 400 h, or 400°C for 250 h.	[2,27]
Alloy 625	$(Ni_{0.9}Fe_{0.1})(Fe_{0.9}Cr_{0.1})_2O_4$.	$(Ni_{0.7}Fe_{0.3})(Fe_{0.2}Cr_{0.8})_2O_4$.	PWR at 260°C for 1,000, 2,000, 5,000, and 10,000 h.	[28]
	$Ni(OH)_2$ and NiO.	Cr_2O_3 and $NiCr_2O_4$.	SCWR at 400°C, 450°C, and 500°C for 250 h.	[29]
	$Ni(Cr, Fe)_2O_4$ spinels.	$Ni(Cr, Fe)_2O_4$ spinels and Cr_2O_3.	SCWR at 400°C and 600°C and 24.8 MPa for 100, 300, and 1,000 h.	[30]
Alloy 690	$(Ni, Fe)Fe_2O_4$ and $(Ni, Fe)(Fe, Cr)_2O_4$ spinels.	NiO.	High-temperature water at 290°C and 10 MPa for 400 h.	[31]
	$Ni_{(1-z)}Fe_{(2+z)}O_4$.	$Ni_{(1-x)}Fe_xCr_2O_4$.	PWR at 325°C and 15.5 MPa for 406 h.	[32]
	NiO and $NiFe_2O_4$ spinels.	Cr_2O_3.	SCWR at 360°C for 2,000 h, 390°C for 400 h, or 400°C for 250 h.	[2,27]
	NiO and Fe-Ni spinels.	NiO and Cr-rich oxides.	SCWR at 400°C, 450°C, 500°C, and 550°C.	[17]
	NiO or $NiFe_2O_4$ spinels, NiO and $Ni(OH)_2$.	Cr_2O_3 and $NiCr_2O_4$ spinels.	SCWR at 450°C and 550°C and 25 MPa for 500 h.	[33]
Alloy 690 TT	Fe-rich spinels and NiO.	Ni-rich oxides.	PWR at 325°C and 15 MPa for 720 h.	[34]
	Fe-rich oxide.	Cr-rich oxide.	SCWR at 500°C and 25 MPa for 500 h.	[35]

LWR, light water reactor; PWR, pressurized water reactor; SCWR, supercritical water reactor; TT, thermally treated.
CrO, chromium (II) oxide; Cr_2O_3, chromium (III) oxide; Fe, iron; $FeCr_2O_4$, iron (II) chromite; Fe_3O_4, iron (II, III) oxide; $NiCr_2O_4$, chromium nickel oxide; $NiFe_2O_4$, nickel ferrite or nickel iron oxide; NiO, nickel (II) oxide; $Ni(OH)_2$, nickel (II) hydroxide.
For more details of water chemistry or processing conditions, please refer to the original articles.

outer oxides, filling the open cracks. A typical example of a 5% cold-worked (CWed) STS 304 sample is shown in Fig. 3 [42].

(2) In the discrete outer oxides, nanoscale Fe-rich M_3O_4 spinels were found to be the major oxide phases for STS 304, STS 304L, STS 316, and STS 316L, whereas nanoscale NiO was determined to be the major oxide phase for Alloy 600, Alloy 600 TT or SA (solution annealed), Alloy 690, and Alloy 690 MA (mill annealed).

(3) In the continuous inner oxides, nanoscale Cr-rich M_3O_4 spinels were identified as the major oxide phase for STS 304, STS 304L, STS 316, and STS 316L, whereas nanoscale Cr_2O_3 was the major oxide phase for Alloy 600, Alloy 600 TT or SA, Alloy 690, and Alloy 690 MA. In addition, such Cr-rich oxides were not produced on common IG carbides but were always around these carbides [57] and tended to concentrate ahead of the crack tip, as shown in Fig. 4 for 10% or 20% CWed STS 304 samples [42] and Fig. 5 for a 20% prestrained Alloy 690 sample [2].

(4) The IG cracking is consequently regarded to be the result of, first, the decrease in yield strength of the GB regions, which were oxidized [12] or corroded [58,59], or the reduction in the tensile strength or shear strength and cohesive energy of the GB regions, which were embrittled by segregated S element [60—62] and secondly, by the strain-induced brittle fracture of the nanoscale continuous inner Cr-rich oxides or the interface between the brittle Cr-rich oxides and the ductile alloy bulk. Typical elastic shear strains and elastic normal strains around the crack tip were observed in the mesoscale in the 5%, 10%, and 20% CWed STS 304 samples [63].

The fracture of brittle Cr-rich oxides is consistent with the classic internal oxidation mechanism [1,57,64] and is supported by both the nanoscale fracture bands within the Cr-rich oxides

Table 3
Statistical comparison in IG corrosion behavior of austenite alloys in simulated LWRs.

Base materials	Major oxide phases	GB elements segregation	Microplastic deformation	Test conditions	Characterization tools	References
STS 304	Fe$_{1-x}$Ni$_x$Cr$_2$O$_4$ spinels or Cr-rich oxides;	Ni enrichment and Cr depletion ahead of GB oxides.		PWR at 360°C for 1,500 h with 20% CW.	APT, ATEM with EDS.	[39]
	Inner Cr-rich and outer Fe-rich spinels.		Oxidized deformation bands intersecting crack surfaces.	PWR at 320°C for 666 h with 5, 10, or 20% CW.	APT, ATEM with EDS, FIB 3-D slicing, NanoSIMS.	[40—42]
STS 304 and STS 304L	FeCr$_2$O$_4$ and Fe$_3$O$_4$ and Cr$_2$O$_3$.		Oxidized deformation bands intersecting crack surfaces; Strain-localized deformation bands with ~100 nm fracture band in crack-tip oxides.	BWR at 288°C and 8.4 or 8.5 MPa.	APT, ATEM with EDS.	[43]
	Inner Cr-rich spinels.	Cr-enrichment in the crack-tip oxides.	Oxidized shear bands intersecting crack tips.	BWR at 288°C for 5000 or 5900 h with 20% CW.		[44]
STS 316	Inner Cr-rich spinels and outer Fe$_3$O$_4$.	Unilateral Ni enrichment ahead of GB oxides.		PWR at 320°C for 500 h.	ATEM with EDS.	[14]
	Inner Cr-rich and outer Fe-rich spinels.			PWR at 360°C for 720 h with 20% CW.	APT, ATEM with EDS, TKD or t-EBSD.	[45,46]
			GB migration.	PWR at 360°C for 700 h with 20% CW and PWR at 345°C for 1500 h.		
			Oxidized twin bands and shear bands intersecting crack surfaces or crack tips.	BWR at 250—290 °C for many years.	ATEM with EDS, NanoSIMS.	[47]
STS 316 and STS 316L	Inner Cr-rich and outer Fe-rich spinels;			BWR at 288 °C for 5000 or 5900 h with 20% CW.	APT, ATEM with EDS.	[44]
Alloy 600	Cr$_2$O$_3$ and NiO.	Cr-enrichment and fine porosities in crack-tip oxides.	Fine porosity in the oxides ahead of crack tip.	PWR at 330 °C for many years.	ATEM with EDS, NanoSIMS.	[47]
				PWR.	ATEM with EDS.	[48]
		Unilateral GB Cr depletion and Ni enrichment ahead of crack-tip oxides.	Fine porosity in the oxides ahead of crack tip.			[49]
	Cr-rich oxides.		Fine porosity in the oxides ahead of crack tip. Oxidized deformation bands intersecting the bulk from the surfaces.	PWR steam at 400 °C for 500 h or at 500 °C for 66 h with 15% CW.	ATEM with EDS, FIB 3-D slicing.	[50]
	Cr$_2$O$_3$.			PWR at 325 °C and 15.86 MPa for 3600 h.	ATEM with EDS.	[51]
	Cr$_2$O$_3$ and NiO.	Cr-enrichment and fine porosities in crack-tip oxides.		PWR at 330 °C and 15 MPa for 1538 and 11,358 h.		[52]
	Cr-rich oxides.	Unilateral GB Cr depletion and Ni enrichment ahead of crack-tip oxides.	Fine porosity in the oxides ahead of crack tip; GB migration.	PWR at 325°C for 500 h.	APT, ATEM with EDS.	[53]
Alloy 600 (TT or SA)	Cr-rich oxides.			PWR steam at 480 °C and 0.1 MPa for 120 h.	ATEM with EDS.	[54]
		Unilateral GB Cr depletion and Ni enrichment before IG cracking.		H$_2$ steam at 480 °C and 0.1 MPa for 120 h.	Scanning transmission electron microscope-electron backscatter diffraction (STEM-EDS).	[55]
Alloy 690	Inner Cr$_2$O$_3$ and outer NiO.	Unilateral GB Cr depletion ahead of crack-tip oxides.	GB migration.	SCWR at 360 °C for 2000 h, 390 °C for 400 h, or 400 °C for 250 h with 20% prestrain.	ATEM with EDS, SEM.	[2,27]
				PWR.	ATEM with EDS.	[51]
Alloy 690 MA			GB migration.	PWR at 360 °C for 1000 h with 20 or 26% CW.		[21]
			Fine porosity in the oxides ahead of crack tip.	PWR at 320 °C for 21,838 h and 360 °C for 20,653 h with 20% CW.	SEM.	[56]

3-D, 3-dimensional; APT, atom-probe tomography; ATEM, analytical transmission electron microscopy; BWR, boiling water reactor; CW, cold work; EBSD, electron backscatter diffraction; EDS, energy dispersive X-ray spectroscopy; FIB-SEM, focused ion beam—scanning electron microscope; GB, grain boundary; IG, intergranular; LWR, light water reactor; MA, mill annealed; PWR, pressurized water reactor; SA, solution annealed; SEM, scanning electron microscope; SCWR, supercritical water reactor; TT, thermally treated.

Cr, chromium; CrO, chromium (II) oxide; Cr$_2$O$_3$, chromium (III) oxide; Fe, iron; FeCr$_2$O$_4$, iron (II) chromite; Fe$_3$O$_4$, iron (II, III) oxide; NiO, nickel (II) oxide.

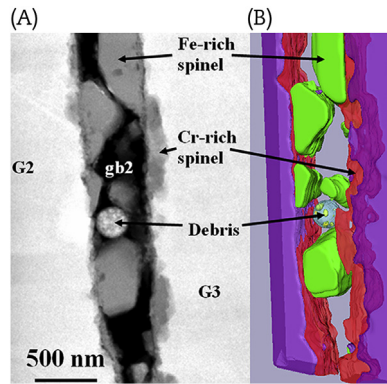For more details of water chemistry or processing conditions, please refer to the original articles.

Fig. 3. The nanoscale IG corrosion of a 5% CWed STS 304 sample exposed to a PWR (500 ppm B, 2 ppm Li, 30 cc-STP/kg-H_2O dissolved H_2) at 320°C for 666 h. (A) The high angle annular dark field (HAADF) image of the duplex IG oxides, including the inner dense Cr-rich spinel layer and the outer Fe-rich spinel layer. (B) The 3-D reconstruction of the topological structure of the duplex oxides in the HAADF image [42] (Reprinted with permission from Elsevier).
CW, cold work; GB, grain boundary; IG, intergranular; PWR, pressurized water reactor.
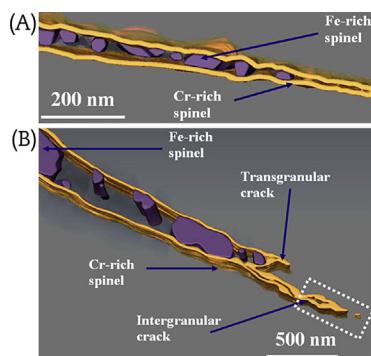
Fig. 4. The 3D reconstruction of the topological structure of the nanoscale duplex IG oxides, including the inner dense Cr-rich spinel layer and the outer Fe-rich spinel layer within (A) 10% or (B) 20% CWed STS 304 samples exposed to PWR (500 ppm B, 2 ppm Li, 30 cc-STP/kg-H_2O dissolved H_2) at 320 °C for 666 h (For interpretation of the references to color in this figure legend, the reader is referred to the web version of this article.) [42] (Reprinted with permission from Elsevier).
CW, cold work; IG, intergranular; PWR, pressurized water reactor

ahead of the crack tip in the STS 304L sample, as shown in Fig. 6 [43], and by the fine porosity in the oxides ahead of the crack tip in Alloy 600 samples [47,49,50,53] and Alloy 690 TT samples [56]. The latter fracture of the interface between the brittle Cr-rich oxides and the ductile alloy bulk, as shown in Fig. 7A, has been newly reported by Dugdale et al [57] and is typically contrary to David E.J. Armstrong's finding, shown in Fig. 7B, which instead agrees with the classic internal oxidation mechanism [1,64,65].

(5) Near the IG crack edge flank, nanoscale (in terms of displacement) GB migration was reported, as shown in Fig. 5, except for STS 304 and STS 304L [2,21,46,53]. Furthermore, this GB migration in supercritical water reactor (SCWR) appeared more dominant in Alloy 600 SA than in Alloy 600 TT [66]. Ahead of the crack tip, Cr-rich oxides, nanoscale unilateral Cr depletion, and Ni enrichment (in other words, elemental segregation) were all found along the GB. Typical examples are shown in Fig. 8 of 20% prestrained Alloy 690 sample [2] and in Fig. 9. The so-called unilateral Cr depletion means that Cr depletion occurs exclusively on one side of the GB plane, instead of both sides, as shown in Fig. 9 [67].
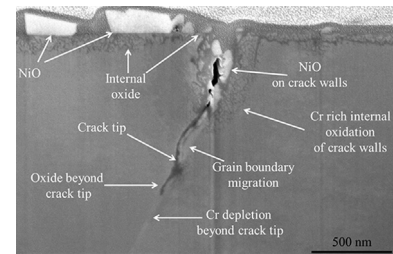

Fig. 5. The 5 keV FIB-SEM cross section of the nanoscale IG corrosion and cracking in a 20% prestrained Alloy 690 sample strained in hydrogenated subcritical water at 360°C to 7% at 5×10^{-8} s^{-1} [2] (Reprinted with permission from Springer).
FIB-SEM, focused ion beam-scanning electron microscope; IG, intergranular.

This elemental segregation, also found in the subsurface region before IG cracking [13,55], as shown in Figs. 2 and 10, is consequently regarded to result from the nanoscale short-circuit diffusion of Cr atoms through GB or dislocation cores to the crack tip and surface regions [68,69] and from the subsequent selective Cr-involved oxidation around the crack tip and surface regions. Furthermore, because the Cr atom has a faster short-circuit diffusion, the original GBs migrate preferentially into one of two neighboring grains, leaving in their wake a unilateral Cr-depleted, Ni-rich zone [67]. Given this, the GB migration during the IG corrosion which features the GB Cr depletion is specifically termed diffusion-induced GB migration [67,70—72].

The qualitative driving force for this short-circuit diffusion of Cr atoms should be the composition gradient of Cr atoms between the unoxidized GB region with higher Cr concentration and the surface region with lower Cr concentration for the surface or IG oxidation in Fig. 10 [55] or between the GB region without Cr depletion (~5.4 at.% Cr in Ni—5Cr binary alloy) and that with Cr depletion (e.g., < 0.05 at.% Cr 100 nm ahead of the IG Cr-rich oxide, or ~0.9 at.% Cr ~2 μm or ~9 μm ahead of IG Cr-rich oxide as shown in Fig. 11 [67]).

(6) The mesoscale plastic deformation bands produced by cold work (CW) were found to be preferentially oxidized, intersecting the crack surfaces or the crack-tip regions, as illustrated by the 20% CWed STS 304 samples in Fig. 12, [42—44,47,63,73]. Such preferential oxidation of the deformation bands was presumed to result from both the increased reactivity of the bulk alloy due to the enhanced strain energy (e.g., the higher dislocation density in the twin deformation bands in the 5% CWed STS 304 sample as shown in Fig. 13 [42]) and the increased diffusivity of O by short-circuit diffusion within the deformation-induced dislocation cores [58].

3. Discussion

3.1. Intrinsic causes of the multiscale nature of SCC

The observed multiscale nature of SCC argues that the SCC of austenite alloys in high-temperature water is produced by interaction between the corrosion of ductile alloys and the cracking of brittle corrosion products (also known as brittle oxides) via the following four qualitative steps, as schematically described in Fig. 14.

- Step 1: Surface or IG corrosion, from Figs. 14A to 14 B:

Duplex surface oxides and an IG Cr-rich oxide monolayer are produced during surface and IG corrosion (also found in Figs. 1, 2, and 10). This is accompanied by the generation of a tensile or shear stress/strain field between the surface oxides and the subsurface
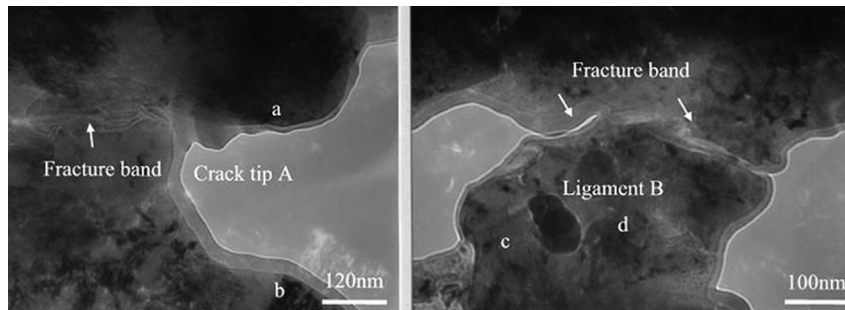
Fig. 6. The cross-sectional ATEM of the nanoscale intergranular SCC crack tip and the fracture bands in the crack-tip oxide in a 5% precracked compact tension (CT) STS 304L sample (with heat treatment at 650°C for 100 h + air cooling + 620°C for 100 h + air cooling) exposed to a BWR (>20 ppm dissolved O$_2$) at 288°C and 8.4 MPa [43] (Reprinted with permission from Elsevier).
ATEM, analytical transmission electron microscopy; BWR, boiling water reactor; SCC, stress corrosion cracking.

alloy bulk and by elemental segregation (Cr depletion and Ni enrichment) produced in the subsurface or GB regions (also found in Figs. 2, 9—11) [1,2,13,14,27,55,63,67]. In addition, the yield or tensile strength of the oxidized or corroded GB regions is reduced [12,59].

- Step 2: Cracking of the surface oxides and further IG corrosion, from Figs. 14B to 14C:

With stress concentration, dislocations slip in the ductile alloy bulk and induce tensile or shear strain, which cracks the brittle surface oxides (also found in Fig. 1) [1,2,14,27,63]. In the meanwhile, IG corrosion progresses by Cr-involved oxidation and produces the inner dense oxide layer of Cr-rich oxides (also found in Figs. 3, 4, 5, 7A, and 8) [2,42,57].

- Step 3: Cracking of IG oxides and further IG corrosion, from Figs. 14C to 14D:

Dislocations slip around the IG oxides and again induce tensile or shear strain, which cracks the IG brittle Cr-rich layer, or the interface between the Cr-rich oxides and the alloy bulk (also found in Figs. 3—5, 7, and 8) [1,2,42,57,63,65]. During such cracking of the IG Cr-rich oxides, diffusion-induced GB migration occurs (also found in Fig. 5) [2,67]. Meanwhile, IG corrosion progresses both by the initial Cr-involved diffusion—oxidation reaction that produces the inner dense oxide layer and by the subsequent Fe- or Ni-involved corrosion/oxidation that produces the outer rough oxide layer (also found in Figs. 3, 4, and 8) [2,27,42,55]. Further elemental segregation continues because of further IG corrosion/oxidation.

- Step 4: Crack-tip corrosion and cracking of crack-tip oxides, from Figs. 14D to 14E:

Crack-tip Cr-involved oxidation preferentially occurs in high-energy structural defects such as the high-angle GBs and deformation bands with high-density dislocations (or strain energy) (also found in Figs. 5, 8, 9, and 12) [2,42,67]. Then the crack-tip brittle Cr-rich oxides refracture via the coalescence of microvoids under the tensile or shear strain produced by the dislocation slipping [43,47,49,50,53,56]. Meanwhile, IG corrosion progresses further, as described in Step 3.

Considering these four qualitative steps, the intrinsic causes of the multiscale nature of SCC in austenite alloys in high-temperature water can be discussed.

- Corrosion/oxidation mechanism:

The mechanism of surface or IG corrosion/oxidation was confirmed to be consistent in the temperature range of boiling water reactor, pressurized water reactor, and supercritical water reactor, and its oxidation rate reasonably increases with increasing operating temperature [2,27]. The duplex surface or IG oxides tend to support the dissolution—precipitation mechanism for the outer Fe- or Ni-rich M$_3$O$_4$ spinels and the diffusion—oxidation mechanism for the inner Cr$_2$O$_3$ or CrO or NiO.

The dissolution mechanism involves the electrochemistry-induced selective dissolution of metal atoms into the high-temperature water and the production of relatively more Fe^{2+}, Fe^{3+}, Ni^{2+} by Equation (1) in Table 4, where M indicates Fe or Ni [33]. This process has been termed electrochemical corrosion, and
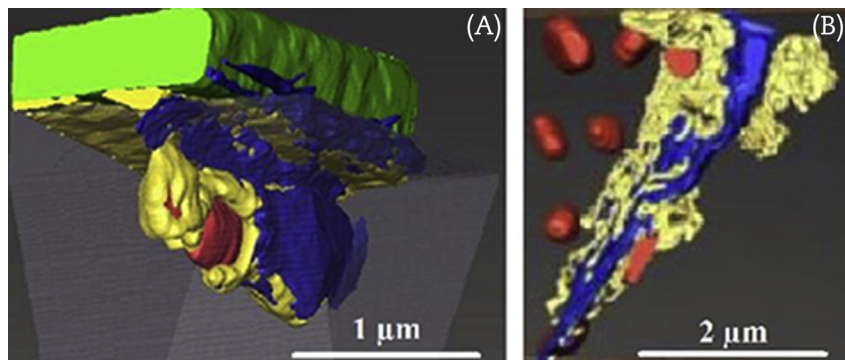

Fig. 7. 3-D reconstruction. (A) Intergranular cracking (blue) through the interface (blue) between Cr-rich oxide (yellow) and alloy bulk (semitransparent) in Alloy 600 exposed to a PWR (2.75 ppm dissolved H$_2$, 500 ppm B and 2 ppm Li) at 360°C for 2,700 h [57]. (B) Intergranular cracking (blue) through the Cr-rich oxides (yellow) in Alloy 600 exposed to a PWR (30 kPa hydrogen partial pressure) at 325°C for 4,500 h [65] (For interpretation of the references to color in this figure legend, the reader is referred to the Web version of this article.) (Reprinted with permission from Elsevier).
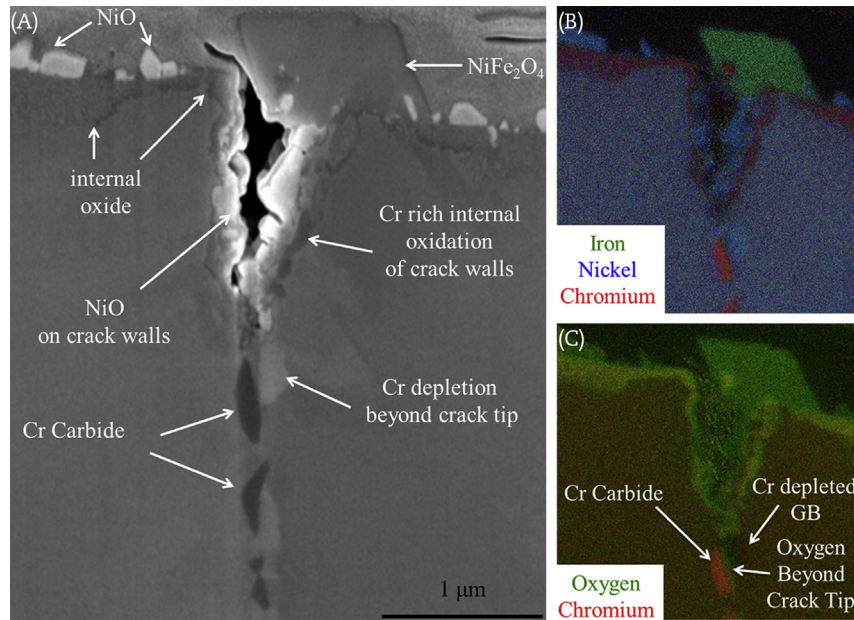
Fig. 8. (A) The 5 keV FIB-SEM cross section of the nanoscale intergranular corrosion and cracking in a 20% prestrained Alloy 690 sample strained in hydrogenated supercritical water at 400°C to 7% at 5×10^{-8} s^{-1} with the corresponding scanning Auger microscopy maps highlighting (B) The metallic composition of duplex intergranular oxides, which include the inner Cr-rich oxide layer and the outer Ni-rich oxide layer (mainly NiO). (C) The presence of oxygen and the elements segregation beyond the crack tip [2] (Reprinted with permission from Springer).
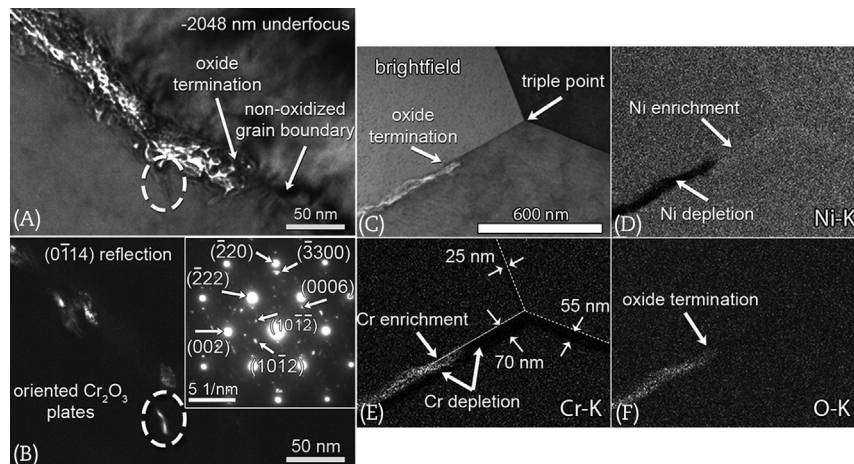FIB-SEM, focused ion beam-scanning electron microscope; GB, grain boundary.

Fig. 9. TEM image. (A) Underfocused brightfield TEM image of the terminal region of intergranular oxidation with the production of Cr_2O_3. (B) Conventional darkfield TEM image of the terminal region of intergranular oxidation with the production of Cr_2O_3. (C-F) scanning transmission electron microscope-electron backscatter diffraction (STEM–EDS) elemental maps of the same grain boundary reveal localized partitioning of Cr to the oxidized region and depletion of Cr from the surrounding grain boundaries in a Ni-5Cr binary alloy exposed to PWR (1000 appm B, 2 appm LiOH) at 360 °C for 1000 h. Note that the STEM–EDS maps in (C-F) are rotated counterclockwise by ~70° relative to panels (A) and (B). [67] (Reprinted with permission from Elsevier).
PWR, pressurized water reactor; TEM, transmission electron microscopy.

it can be verified by evaluating the amount of weight loss, the anodic polarization curves, or the electrochemical corrosion potential [74–76].

The precipitation mechanism refers to the precipitation of metal hydroxides $Fe(OH)_2$ or $Ni(OH)_2$ back onto the surfaces and the production of the outer M_3O_4 spinels oxides listed in Table 2, such as Fe_3O_4 and $FeNi_2O_4$ for Fe-base alloys and $NiFe_2O_4$ for Ni-base alloys by Equations (2–3) in Table 4 [33]. The source of the Cr^{3+} in the inner $FeCr_2O_4$ or $NiCr_2O_4$ may be from the original surface passive film of Cr_2O_3 or the inner subsurface Cr_2O_3, newly produced by the diffusion–oxidation reaction. The reactive molecular dynamics simulation using the ReaxFF interatomic potential indicated the formation of Cr-OH, when load-free Cr_2O_3 was exposed to

high-temperature water ranging from 526.85°C to 1726.85°C [77,78]. Furthermore, the reported thermodynamic stability of oxides in the order $Cr_2O_3 > FeCr_2O_4 > NiCr_2O_4 > NiFe_2O_4 > NiO$ may imply possible reactions by Equations (4–5) in Table 4, which may result in the observed IG Cr-rich spinels e.g., $NiCr_2O_4$ and $FeCr_2O_4$ [33,79,80].

NiO can be produced by the diffusion–oxidation mechanism [81], whereas FeO has not been directly observed and may be from an isolated surface Fe_3O_4 ($FeO·Fe_2O_3$) particle, which is often observed in the early stage of surface corrosion. This selective dissolution can also be correlated with the appearance of micro-scale porous features on the outer oxide layer, which does not provide further protection against corrosion. The precipitation may
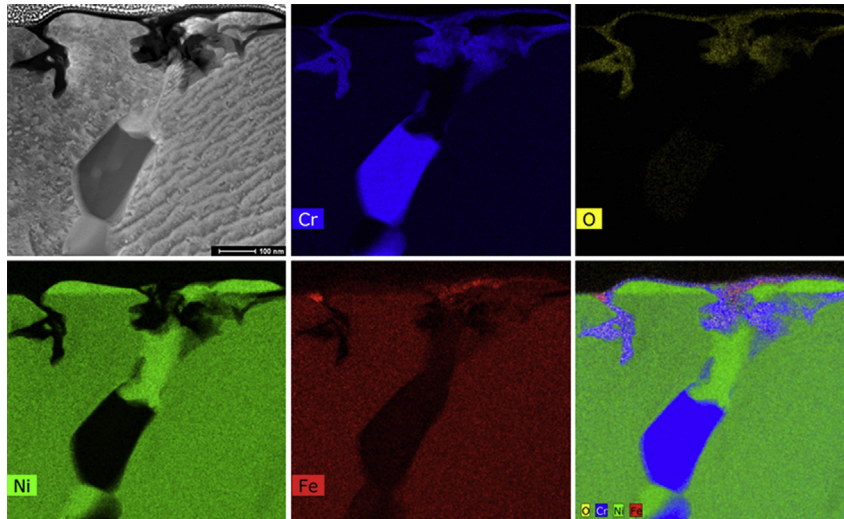
Fig. 10. Scanning transmission electron microscope-high angle annular dark field image and corresponding STEM-EDS spectrum images of an oxidized high-angle grain boundary in Alloy 600 TT exposed to H_2 steam at 480°C for 120 h, with subsurface or grain boundary elements segregation (Cr depletion, Fe depletion, and Ni enrichment) before intergranular cracking [55] (Reprinted with permission from Elsevier).
TT, thermally treated.

be a random or anisotropic process, and this is supported by the jagged cross section of the outer oxide layer shown in Fig. 2. The interface between the outer Fe- or Ni-rich oxides and inner Cr-rich oxides was found to match the original alloy surface before being corroded [17]. This phenomenon may be balanced by the faster diffusion (and thus the faster dissolution−precipitation) of Fe ions in the spinel oxide (Fe^{3+}>Fe^{2+}>Ni^{2+}>Cr^{3+}) [17,41] and the Cr atom's larger susceptibility to oxidation, which is discussed in the following section by the standard reduction potential [82], and the preferential thermodynamic stability of Cr_2O_3 [33].

The diffusion−oxidation mechanism means the surface or GB oxidation of Cr or Ni atoms (namely, the production of Cr_2O_3 or CrO or NiO) via three consecutive processes: (i) the diffusion of an oxidizer (O^{2-} and O atom from O_2, H_2O, or H_2O_2) onto the original surface passive film (Cr-rich oxide); (ii) diffusion through the passive film; and (iii) oxidation at the surface oxide−alloy interface or at the GB region [83]. The diffusion can be accelerated by short-circuit paths, such as the GBs and CW-induced deformation bands, which have more vacancies and dislocations. This process is called short-circuit diffusion. The short-circuit diffusion indicates not only the inward diffusion of oxidizing species, e.g., O^{2-} and O atoms, but also the outward diffusion of metal atoms via GB or dislocation cores [17,31,33,36,79,80]. In addition to the obvious O profile, the diffusion−oxidation mechanism can also be supported by the frequently observed subsurface or GB Cr depletion [2,13,27,55], as shown in Figs. 2, 8, and 10, as well as the oxidation scale for different dislocation densities or GB types or implanted cavities [42,51,84,85].

For both the outer Fe- or Ni-rich oxides, which are produced by the dissolution−precipitation mechanism, and the inner Cr-rich oxides, which are produced by the diffusion−oxidation mechanism, the corrosion/oxidation activity can occur in a sequence such as $Cr^{2+} > Cr^{3+} > Fe^{2+} > Ni^{2+} > Fe^{3+}$ according to the corresponding standard reduction potential: -0.913 V (Cr^{2+}) < -0.744 V (Cr^{3+}) < -0.447 V (Fe^{2+}) < -0.257 V (Ni^{2+}) < -0.037 V (Fe^{3+}) [82]. The common IG Cr depletion can also be induced by the GB diffusion of the Cr atom because it has lower activation energy than that of Fe or Ni atoms in the vacancy diffusion mechanism. A comparison is shown in Table 5 [86]. The protective surface Cr_2O_3 film that appears before surface cracking, or the penetrative CrO in Alloy 600

and Alloy 690, can be produced by this diffusion−oxidation mechanism [2,27,36].

• Short-circuit diffusion and diffusion-induced GB migration

As confirmed by the Cr-involved diffusion−oxidation reaction and IG Cr depletion shown in Figs. 5, 8, 10, and 12, the short-circuit diffusion of Cr or O atoms mainly refers to the GB or dislocation pipe diffusion of Cr or O atoms and features a higher diffusivity, in the following order: $D_s > D_{hgb} > D_{lgb} \approx D_{ud} > D_{dd} > D_l$, where D_s, D_{hgb}, D_{lgb}, D_{ud}, D_{dd}, and D_l represent the diffusivity on the surface, high-angle GBs, low-angle GBs, undissociated dislocation, dissociated dislocation, and lattice, respectively [68,87]. Because they are sources or sinks of vacancies, the GB core and the dislocation pipe core can provide more free space for diffusion, and therefore require lower diffusion activation energy. Aided by these structural paths, both the vacancy diffusion mechanism and the interstitial diffusion mechanism can be the short-circuit mechanisms for GB diffusion, whereas the vacancy−interstitial pair mechanism is the mechanism for dislocation pipe diffusion.

Recent modeling work has reported that the vacancy diffusion mechanism is dominant for the GB diffusion of Cr or Fe atoms in Fe-Cr-Ni austenite alloys under the simultaneous thermal and irradiation conditions of LWRs, whereas for the Ni atom, the interstitial diffusion mechanism is highly competitive with the vacancy diffusion mechanism under the same conditions [88]. The diffusion of O atoms in the Ni bulk was also reported to be a vacancy−interstitial (O) pair mechanism [81].

Diffusion in the $\sum 5$ [001] tilt GB with a tilt angle of 36.9° in body-centered cubic Fe shown in Fig. 15A is a typical example of GB diffusion. It can occur by the following three possible mechanisms: (i) By vacancy diffusion mechanism, a vacancy inserted at site B, marked by the left arrows, preferentially jumps among sites A, B, C, and D rather than into the sites E, F, and G, which are farther away from the GB midplane; (ii) By interstitial diffusion mechanism, the diffusion atom at site B, marked by the middle arrow, can jump into the interstitial site I, therefore creating a GB interstitial and a GB vacancy; (iii) By ring mechanism, marked by the right arrows, that can involve both the interstitial mechanism from atom B to interstitial I and the vacancy mechanism from atom B' to vacancy B [68].
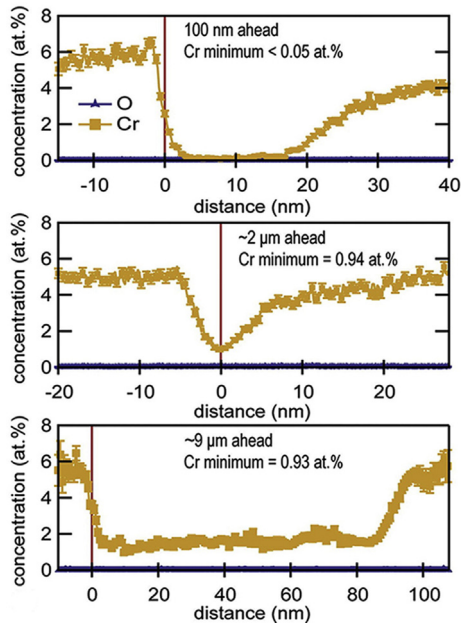
Fig. 11. 1-D concentration profiles of Cr atom from APT analysis across the grain boundary (red line) and Cr-depleted zone 100 nm or ~2 μm or ~ 9 μm ahead of intergranular oxidation front in a Ni—5Cr binary alloy exposed to a PWR (1,000 ppm B, 2 ppm LiOH) at 360°C for 1,000 h. Error bars indicate one standard deviation from the counting statistics [67]. (Reprinted with permission from Elsevier). (For interpretation of the references to color in this figure legend, the reader is referred to the Web version of this article.)
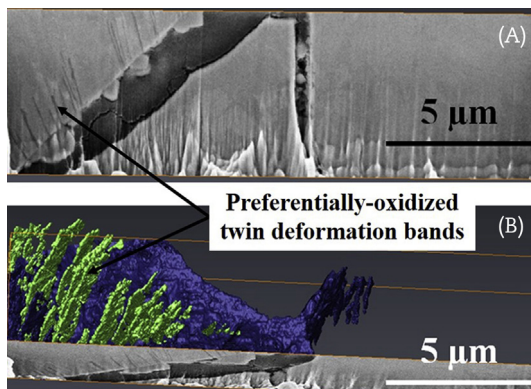APT, atom-probe tomography; PWR, pressurized water reactor.

Fig. 12. (A) The SEM SE image of the mesoscale preferentially oxidized twin deformation bands (darker contrast on the top grain) intersecting the crack surfaces of a 20% cold-worked STS 304 sample exposed to a PWR (500 ppm B, 2 ppm Li, 30 cc-STP/kg-H$_2$O dissolved H$_2$) at 320°C for 666 h. (B) The corresponding 3-D reconstruction model showing the volume of the open crack (dark or blue) and the oxidized twin deformation bands (light or green), together with one of the original slices (For interpretation of the references to color/colour in this figure legend, the reader is referred to the Web version of this article.) [42] (Reprinted with permission from Elsevier).
PWR, pressurized water reactor; SEM, scanning electron microscopy.

Furthermore, the binding energy of the vacancy or interstitial in the GB core is site dependent. The binding energy of a vacancy can be −1.9, −40, −8.7, and −17 kJ/mol for sites *A, B (B′), C,* and *D (D′)*, respectively, in Fig. 15A. It is much smaller than the 130 kJ/mol calculated to be the formation energy of a vacancy in the lattice. The binding energies of the interstitial are −211, −211, −139, and −234, -355 kJ/mol for sites *A, B (B′), C,* and *D (D′)*, respectively. It is also much smaller than the 458 kJ/mol that was calculated to be the formation energy of the interstitial in the lattice [68,71].
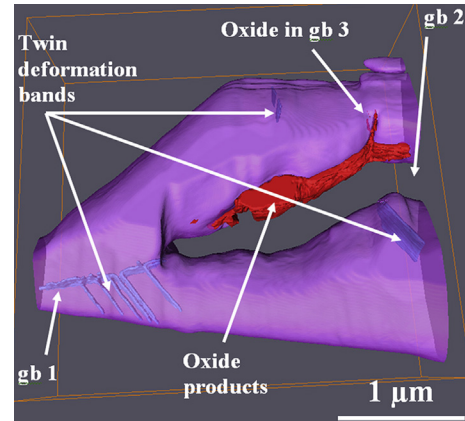

Fig. 13. The 3-D reconstruction model of a mesoscale IG crack with the mesoscale twin deformation bands with higher dislocation density intersecting the crack-tip regions in a 5% CWed STS 304 sample exposed to a PWR (500 ppm B, 2 ppm Li, 30 cc-STP/kg-H$_2$O dissolved H$_2$) at 320°C for 666 h [42] (Reprinted with permission from Elsevier). CW, cold work; GB, grain boundary; IG, intergranular; PWR, pressurized water reactor.

More site-to-site comparisons of vacancy formation energy can be found in the review [89].

The dislocation pipe diffusion mechanism was applied to the diffusion in the dislocation core. The dislocation core is defined as the last line of filled sites in the inserted plane of an edge dislocation, together with the line of vacant sites into which that plane would grow by negative climb. In this dislocation core, shown as a dotted pipe in Fig. 15B, an interstitial is defined as an atom in a row of vacant sites, whereas a vacancy is defined as a vacant site in a line of atoms. Dislocation pipe diffusion takes place when an interstitial atom recombines with a vacancy rather than the one created simultaneously with it, or when net motion occurs for a vacancy—interstitial pair between the creation and annihilation of the vacancy—interstitial pair [90]. Considering the thermal-activation or site (or defect path)-dependent nature of diffusion [91—93], and therefore the temperature-accelerated corrosion/oxidation ability of supercritical water [2,27,33,94], more analysis is still needed on how the diffusivity or the activation energy of Cr or O atoms affects the mechanism of Cr depletion or IG corrosion. This is particularly important when the operating temperature is increased from boiling water reactor to pressurized water reactor to SCWR conditions and with the interaction of manufacturing-induced defect types or density. More representative mathematical or simulation-assisted discussions on the GB or dislocation pipe diffusion beyond SCC can be found in reviews [95—97].

Diffusion-induced GB migration has already been reviewed [98], although the authors only discuss one classic model for diffusion-induced GB migration [68,71]. As shown in Fig. 15C, a pure edge dislocation is inserted in a tilt GB core with a tilt angle of 36.9° and a core width of λ. When this GB dislocation absorbs a vacancy that is produced during the unequal GB diffusion, it will climb upward by distance *s*. Three atoms, shown in black, are removed from crystal lattice 2, and two of them are added to crystal lattice 1. In this manner, crystal 1 grows at the expense of crystal 2, one vacancy is occupied by the lower single atom, and this is how diffusion-induced GB migration occurs.

Recent works have also reported GB migration produced by dislocation emission and accumulation within the GB core [99,100]. The propagating dislocations mainly refer to the frequently observed dislocations emitting and propagating around the IG crack tip [101,102]. In SCC, however, the GB migration is more complicated because of the oxidation- or cracking-induced lattice distortion. The interaction of propagating dislocations and the
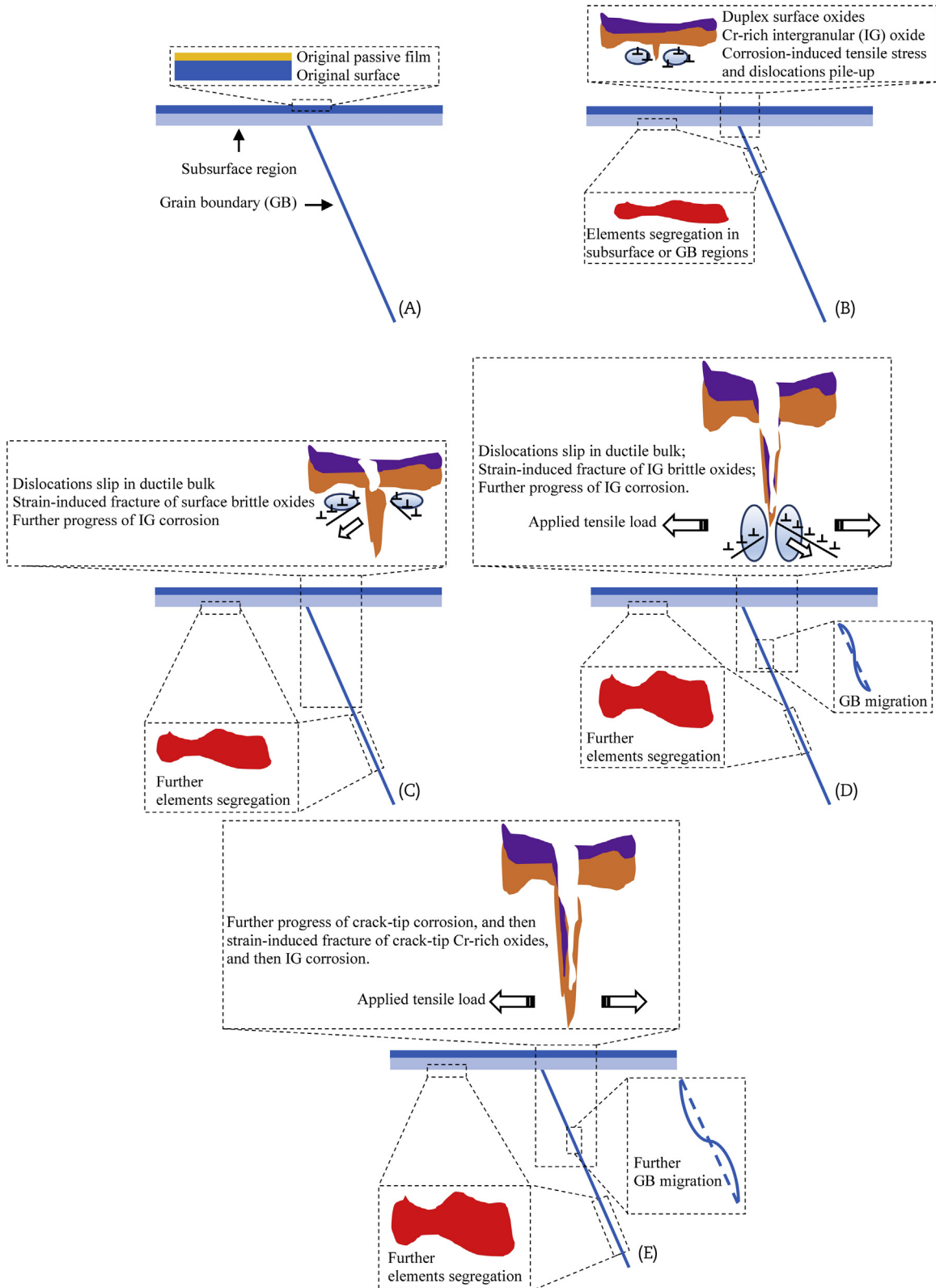
Fig. 14. A proposed qualitative SCC initiation and propagation mechanism of austenite alloys in the high-temperature water based on local topological nature, including the following. (A) The conceptual cross section of as-received austenite alloys with a surface Cr-rich passive film formed in the air. (B) The surface or intergranular (IG) corrosion and elements segregation in subsurface or grain boundary regions. (C) The fracture of duplex surface corrosion products and further IG corrosion. (D) The fracture of IG corrosion products and further IG corrosion. (E) The further crack-tip corrosion and subsequent cracking of crack-tip corrosion products and further IG corrosion.
SCC, stress corrosion cracking.

Table 4
One reported dissolution—precipitation mechanism for surface corrosion [33].

Equations	Number of equations
$M + 2H_2O \rightarrow M^{2+} + 2OH^- + 2H^+ + 2e$	1
$Ni(OH)_2 + 2Fe(OH)_2 \rightarrow NiFe_2O_4 + 2H_2O + H_2$	2
$2Ni(OH)_2 + Fe(OH)_2 \rightarrow FeNi_2O_4 + 2H_2O + H_2$	3
$NiO + Cr_2O_3 \rightarrow NiCr_2O_4$	4
$FeO + Cr_2O_3 \rightarrow FeCr_2O_4$	5

Table 5
Comparison of activation energy (in kJ/mol) for diffusion of alloying elements in Ni via vacancy diffusion mechanism in four representative paths [86] (reprinted with permission from American Chemical Society).

Diffusion paths	Diffusing species in Ni alloys		
	Cr	Fe	Ni
(111) surface	53.06	75.26	88.77
$\Sigma = 9/(221) <110>$ symmetric tilt grain boundary	8.68	27.99	33.77
$\Sigma = 3/(111) <110>$ symmetric tilt grain boundary	58.86	86.84	95.52
Bulk	78.15	91.67	104.2

short-circuit diffusion of Cr or O atoms during IG corrosion and cracking are hereby considered to be cocontributors to the GB migration. However, dynamic proof of such interactions with O atoms during the complicated IG corrosion and cracking is still lacking.

• Aspect 3 Crack initiation and propagation mechanism:

Just as illustrated in Figs. 1, 3—8, 12, and 13, with the occurrence of surface or IG corrosion and the subsequent reduction in yield or tensile or shear strength, and the fracture toughness of the corroded or oxidized parts of interest, surface or IG cracking occurs by a multiscale brittle fracture of the Cr-rich oxides or of the interface between the Cr-rich oxides and alloy bulk. This is generated by the tensile or shear strain within or around the brittle oxides [2,12,14,27,37,38,42,55,57—62,65,103,104,106]. This multiscale fracture process may first start with the rupture of ionic bonds in the oxide molecular templates, from Ångström scale to nanoscale, like the transgranular cleavage fracture on the {111} planes in Si [103,107,108]. Second, it may be induced by the accumulation of ruptured bonds and the coalescence of microvoids at mesoscale (also known as the formation of IG microcracks) [109] and the formation of crack bridges between neighbor IG microcracks, as shown in Fig. 16 [110]. Finally, it may occur due to the fracture of the continuum corrosion film at microscale as a result of the further coalescence of microcracks and the destruction of crack bridges ahead of a propagating mother crack [111,112].

Furthermore, in the second stage, the multiscale fracture process features not only a change from the brittle cleavage in the first stage to the dislocation-facilitated slip failure of the crack-tip oxide but also a reduction in potential energy or tensile stress. This has been typically observed in the SCC of strained Al_2O_3 slab [113].

In the last stage, the crack interactions during crack propagation were confirmed using a combination of qualitative digital image correlation and quantitative phase field calculation [114]. The dynamic fracture instabilities of a highly strained crack tip in brittle materials are governed by hyperelasticity at a critical length scale for the energy flux near the crack tip at nanoscale and can increase the roughening of the fracture surfaces [111,115]. However, the current discussion about the cracking path, either through the Cr-rich oxides or through the interface of Cr-rich oxides and alloy bulk shown in Fig. 7, implies a more complicated cracking activity which interacts with the on-going corrosion/oxidation activity under different water chemistry conditions.

The tensile or shear strain that cracks the brittle oxides ahead of a crack tip, as schematically shown in Figs. 14 and 17, is presumed to be caused by dislocation emission and propagation via slipping, climbing, or dissociation behavior in the notched ductile bulk, locally around the brittle oxides and where there is stress concentration [101,105]. The stress concentration in the local ductile bulk can be caused by both the intrinsic corrosion activities on the surface [38] and within the GBs with different structures [55] and by the application of processing loads. For example, it can occur with (i) welding (e.g., 30—60% residual stress

in the weld metal of STS 304 pipe with overloaded heat input [116,117]; 40—50% residual strains in the weld metal, ~20% in unmixed and partially melted zones, ~15% in the heat-affected zone of Alloy 152, Alloy 52, and Alloy 52i weld metals, and 8—10% in the bulk of Alloy 690 [118]; and 5—25% residual strains in the interface between Alloy 152 weld metal and Alloy 52M weld metal [119]). It has also been reported for (ii) CW (e.g., a higher strain density and increased hardness and hence, higher IG SCC crack growth rate in Alloy 690 plate, tubing, and bar materials by ~17% or more CW [120,121]; high-density transgranular cracks nucleating from surface-corroded TiN stringers and propagating into the 26% cold-rolled Alloy 690 matrix [36]). It is also known for (iii) electrical discharge machining (e.g., a high positive correlation between the initiation rate of SCC and residual stress on STS 316 surfaces [122]).

On the other hand, for CWed Alloy 690 materials, both the before-CW high-temperature annealing at 1100°C followed by water quench and the post-CW recovery annealing at 700°C for 1 hour followed by air cooling can decrease the IG SCC crack growth rate by decreasing the localized GB stress/strain that is produced by the intrinsic IG carbide precipitates or the applied CW [120,121,123—125]. However, owing to limited reports about effects of interactions (or trade-offs) between warm work and CW on IG SCC susceptibility, more systematic heat-to-heat warm work is needed to modify the GB characteristics. This is of critical importance for practically inhibiting IG SCC susceptibility [123,124].

3.2. Questions of interest about the intrinsic causes of the multiscale nature of SCC

Considering the state of research on the intrinsic causes of the multiscale nature of SCC, as discussed previously, there is still a need for an analysis of the temporal and spatial evolution of the multiscale SCC phenomena at different time and length scales. Questions of interest include the following:

(1) With respect to the mechanism of corrosion of a nanoscale surface or GB or crack tip, as shown in Figs. 1—10, 12, and 13, the nanoscale dissolution—precipitation reactions should be dynamically visualized, involving mechanism-related evidence such as the selective dissolution of the metal ions or atoms, the nanoscale precipitation of the metal hydroxides, and the electrons transfer at Ångström scale.

(2) Regarding the mesoscale subsurface or GB elemental segregation (mainly the GB Cr depletion), coupled with the Cr-involved diffusion—oxidation, shown in Figs. 3—10, and the preferential oxidation of deformation bands, shown in Fig. 12, the nanoscale short-circuit diffusion of Cr and O atoms in the dislocations of different density and GBs with different structures and chemical composition should be dynamically visualized to understand the mechanisms behind such changes in local chemistry. This includes
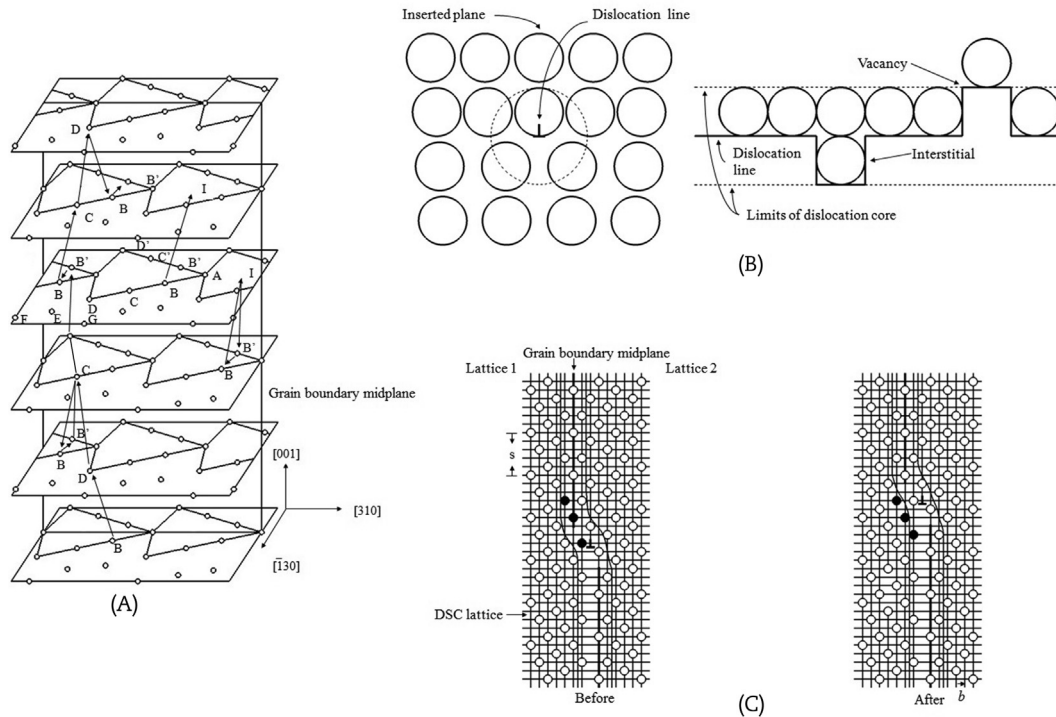
Fig. 15. Atomic models. (A) Atomic model for short-circuit diffusion in $\sum 5$ [001] tilt grain boundary ($\theta = 36.9°$) in bcc iron, calculated by molecular statics and dynamics. The ratio of the scale used in the drawing is [$\bar{1}$30]:[310]:[001] = 1:1:5 [68] (Reprinted with permission from Springer). (B) Atomic model for short-circuit diffusion in a pure edge dislocation pipe in simple cubic lattice by vacancy−interstitial pair mechanism [90] (Reprinted with permission from Elsevier). (C) Atomic model for diffusion-induced grain boundary (GB) migration of $\sum 5$ [001] tilt grain boundary ($\theta = 36.9°$) in bcc iron when a GB dislocation climbs upward by a distance s (per lattice plane parallel to paper) [68,71] (Reprinted with permission from Springer). DSC, displacement shift complete.
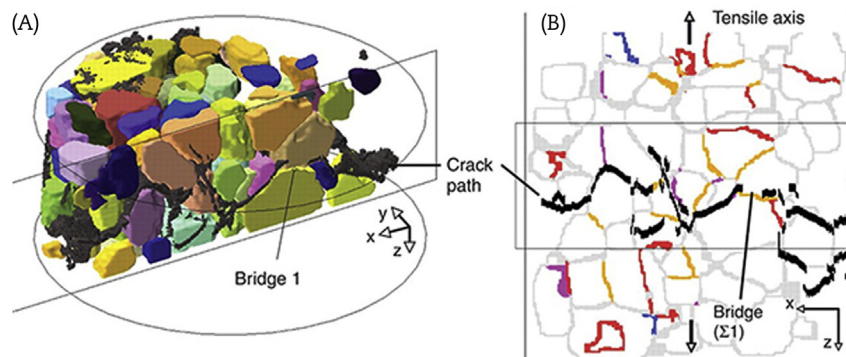

Fig. 16. Combined use of diffraction contrast tomography (DCT) and computed tomography (CT) data to identify crack-bridging grain boundary structure during an intergranular SCC of STS 302 wire (sensitized by solution anneal-treatment at 1,050°C for 30 min and then aged at 650°C for 60 min) exposed to acidified solution of potassium tetrathionate ($K_2S_4O_6$), where (A) Intergranular cracks obtained from CT data are shown in black, at the final step before sample failure, and compared with DCT data of 3-D grain shapes. (B) 2-D section of the grain boundaries, identified by DCT, compared with the crack path identified by CT. A crack bridge is indicated [110] (Reprinted with permission from The American Association for the Advancement of Science).
SCC, stress corrosion cracking.

mechanism-related evidence such as temperature- or stress- or defect-density− or defect-type−dependent diffusivity and diffusion trajectory and activation energy barrier.

(3) With respect to nanoscale GB migration during the IG corrosion and cracking, shown in Fig. 5, the nanoscale stress-dependent dislocation dynamics or interactions along the corroded/oxidized GBs with different structures and chemical composition should be dynamically visualized to understand the mechanism of diffusion-induced GB migration.

(4) With respect to the strain-induced fracture of the surface or IG or crack-tip oxides, the nanoscale stress-dependent

dislocation dynamics or interactions in the unoxidized alloy that bulk around the brittle oxides, as schematically shown in Figs. 13, 14, and 17, should be dynamically visualized to further understand the strain profile and distribution within or around the brittle oxides. Furthermore, the rupturing of ionic bonds of oxide molecule templates at nanoscale, the accumulation of ruptured bonds and the coalescence of microvoids at the mesoscale (in other words, the formation of microcracks), and the fracture of brittle oxide film at microscale on the alloy bulk by the formation and coalescence of microcracks ahead of a propagating
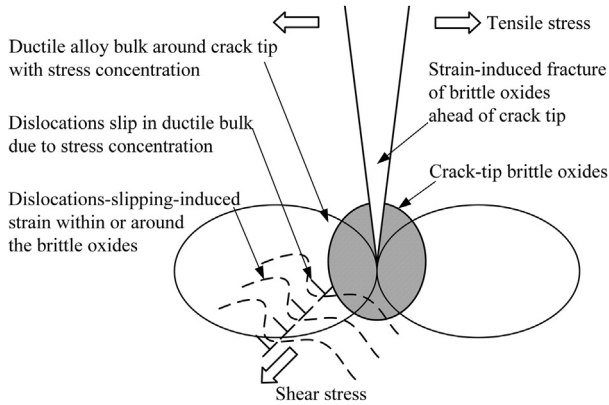
Fig. 17. Schematic process of strain-induced fracture of crack-tip brittle oxides after the dislocations slip in the ductile bulk around the brittle oxides.

mother crack should be dynamically visualized under different stress/strain and chemistry conditions. This would contribute to a multiscale understanding of crack initiation and propagation mechanisms.

Last, the hyperelasticity-dependent dynamic fracture instabilities of a highly strained crack tip in the brittle oxides should be dynamically visualized and quantitatively analyzed to determine a critical length scale for the energy flux near the crack tip during crack propagation.

3.3. Additional approaches to determine the intrinsic causes of the multiscale nature of SCC

Multiscale questions call for multiscale solutions. Multiparadigms and multiscale modeling and simulation have been designed to imitate the temporal and spatial evolution of materials failure [5,126–128], and therefore can be hierarchically proposed as a multiscale solution to investigate the intrinsic causes of the observed multiscale nature of SCC.

(1) *Ab initio* quantum mechanics (QM) and quantum chemistry calculations at Ångström scale based on the density functional theory or Monte Carlo method, as illustrated in Fig. 18A, could quantitatively describe the kinetic electron transfer, formation energy of vacancy or interstitial defects, the ionization potential during the dissolution–precipitation or diffusion–oxidation reactions, and the activation energy barrier for short-circuit diffusion [86,128–136].

(2) Reactive molecular dynamics simulation at nanoscale can be conducted based on reactive force fields such as the popular ReaxFF potential [137,138], charge-optimized many-body potential [139], embedded-ion method potential [140], reactive empirical bond order potential [141], adaptive intermolecular reactive empirical bond-order potential [142], electrostatic potentials [143], and Tersoff potential [144], as illustrated in Fig. 18B. These are capable of capturing the rupturing of ionic bonds and the formation of ionic bonds (or the changing positions of ions or atoms) during the complex chemical reactions, with QM accuracy and lower computational cost. This would enable the dissolution–precipitation or diffusion–oxidation reactions during surface or IG corrosion and the strain-induced rupture of ionic bonds of surface or IG or crack-tip brittle oxides, to be directly understood in relation to measurements such as the temperature- or stress-dependent reactive or cracking rate, crack-limiting speed, crack-tip instabilities, and orientation-dependent cleavage fracture path [59,62,111,138,145–148].

(3) The nonreactive molecular dynamics simulation at nanoscale, as illustrated in Fig. 18C, can physically describe the
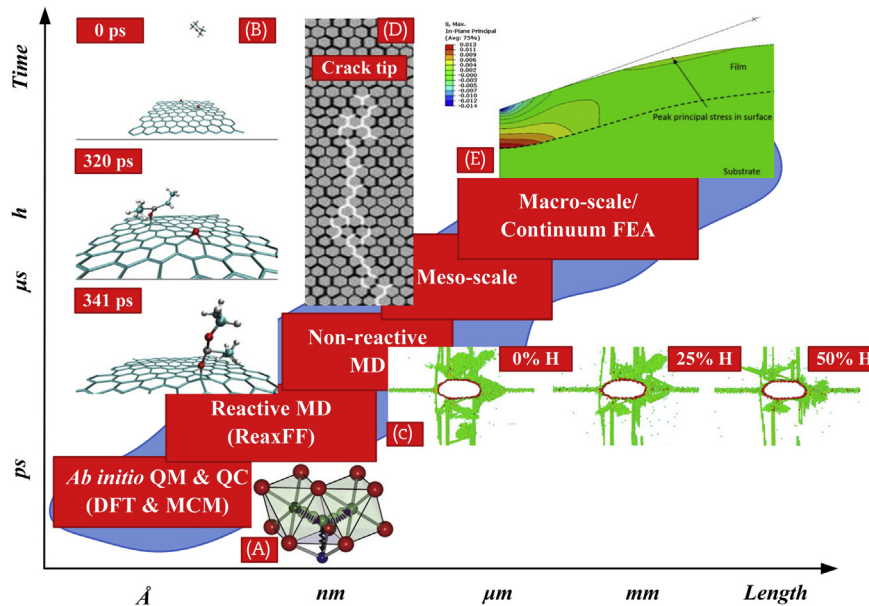

Fig. 18. Conceptual framework of the multiscale and multiparadigm modeling and simulation [5] with their applications including the following. (A) Li (green) moves from one octahedral site to another by passing through an intermediate tetrahedral site where it encounters strong repulsion from a nearby transition-metal cation (blue) [131] (Reprinted with permission from the American Association for the Advancement of Science). (B) A single atomic layer deposition simulation depicts the double oxygen abstraction by diethyl zinc (green-C, white-H, black-Zn, red-O) [148] (Reprinted with permission from the American Chemical Society). (C) Dislocation (green) activity during crack propagation (red ellipse) colored by the centrosymmetry parameter at 10,000 ps with different hydrogen (H) atom coverage at the primary grain boundary [149] (Reprinted with permission from Elsevier). (D) A mesoscale crack (white) propagates in a microstructure (black net) [165] (Reprinted with permission from Elsevier). (E) The principal stress distribution in a brittle thin film on a ductile substrate by finite element analysis (FEA) at microscale [169] (Reprinted with permission from Elsevier) (For interpretation of the references to color in this figure legend, the reader is referred to the Web version of this article.)

DFT, density functional theory; MCM, Monte Carlo method; MD, molecular dynamics; QC, quantum chemistry; QM, quantum mechanics.

atomistic motion behavior and the hyperelasticity of a crack tip in strained brittle oxides and can help explain the nanoscale dislocation dynamics or interactions, and therefore the diffusion-induced GB migration and dynamical fracture instabilities, using evidence such as the defect-density level and stress/strain/energy flow profiles [101,111,115,149,150].

(4) *Ab initio* QM and quantum chemistry calculations and reactive or nonreactive molecular dynamics simulations can all provide insight into the short-circuit diffusion of metal atoms and O atoms in the GB or dislocation cores using data on diffusion trajectory, diffusivity, diffusion flux, and activation energy barriers. The simulation of atomistic diffusion can provide nanoscale insights into elemental segregation, the diffusion-induced GB migration, and short-circuit diffusion/oxidation within the GBs and deformation bands [62,81,83,145,151—158];

(5) Mesoscale simulations, as illustrated in Fig. 18C, can provide insight into nonlocal features during deformation and dynamic failure and link the atomistic simulation at nanoscale to the continuum finite element analysis at microscale [159]. The coupling of multiscale simulations similar to those in Fig. 18 can hierarchically clarify local features. These include ionic bond formation or rupture, atomistic diffusion, and dislocation dynamics or interactions at nanoscale, as illustrated in Figs. 18A—18C; nonlocal features such as the accumulation of ruptured bonds and the evolution of defects at mesoscale, as illustrated in Fig. 18D (for example, GB migration, the interaction of defects, the strain field configuration ahead of a crack tip, the crack-tip propagation, autonomous crack growth, and interaction among multiple microcracks [110,160—168]); and the fracture of thin brittle film at microscale on the ductile alloy bulk [38,169,170], as illustrated in Fig. 18E.

4. Conclusions

High-resolution characterizations have demonstrated that the SCC in austenite alloys in LWRs is due to multiscale interactive processes involving the corrosion of ductile alloys and the cracking of brittle oxides. The surface or IG corrosion of alloys involves the multiscale nature of SCC, such as nanoscale dissolution—precipitation oxidation and diffusion—oxidation, mesoscale elemental segregation (Cr depletion and Ni enrichment), and GB migration. The latter two processes are induced by the nanoscale short-circuit diffusion of metal or O atoms. The surface or IG cracking of brittle Cr-rich oxides, or at the interface between the Cr-rich oxides and alloy bulk, has been shown to result from the reduction in yield or tensile or shear strength of parts of interest, which have been corroded or oxidized on the surface or in GB regions and deformation bands. These can be described as strain-induced multiscale fracture processes, involving the coalescence of microvoids (or the formation of microcracks and crack bridges) at mesoscale, and the final fracture of continuum passive film at microscale by the further coalescence of microcracks and the destruction of crack bridges ahead of a propagating mother crack. Such multiscale cracking procedure also implies the rupture of ionic bonds in molecular oxides, occurring from the Ångström scale to the nanoscale. All the multiscale nature of SCC in LWRs seems to be related to co-contributions from the film-rupture model and the internal oxidation mechanism.

The tensile or shear strain that cracks the brittle oxides is caused by dislocation emissions and propagation in the notched ductile bulk with stress concentration. This local stress concentration can be produced on one hand by the intrinsic corrosion activity but is mostly caused by processing loads, like improper dissimilar

welding, a CW of 15% or more, and electrical discharge machining. On the other hand, it can be reduced by warm works, such as before-CW high-temperature annealing at 1100°C, followed by water quench and a post-CW recovery annealing at 700°C for 1 hour, followed by air cooling. Regarding the role of manufacturing processes in inhibiting the SCC susceptibility, there is still a need for more heat-to-heat experimental investigations on the trade-off between recovery warm work and CW in modifying the GB characteristics.

To gain a better bottom-up understanding of the intrinsic causes of the multiscale nature of SCC, more studies on the temporal and spatial evolution of local chemistry and microstructure need to be performed. Specifically, these should focus on the dissolution—precipitation reactions for the electrochemistry corrosion mechanism; the short-circuit diffusion of Cr, Ni, and O atoms for elemental segregation or the diffusion—oxidation mechanism; the dislocation dynamics or interactions within oxidized GB regions for the diffusion-induced GB migration mechanism; and the rupture of ionic bonds in Cr-rich oxide molecular templates from the Ångström scale to nanoscale for the multiscale cracking mechanism. From this point of view, employing multiparadigms and multiscale modeling and simulation, in synchrony with high-resolution characterizations, is a promising interdisciplinary methodology that can advance understanding of the multiscale nature of SCC in LWRs.

Conflicts of interest

All authors have no conflicts of interest to declare.

Acknowledgments

References

[1] S. Lozano-Perez, J. Dohr, M. Meisnar, K. Kruska, SCC in PWRs: learning from a bottom-up approach, Metall. Mat. Trans. E 1 (2014) 194—210.

[2] T. Moss, G.S. Was, Accelerated stress corrosion crack initiation of alloys 600 and 690 in hydrogenated supercritical water, Metall. Mat. Trans. A 48 (2017) 1613—1628.

[3] X.Y. Zhong, S.C. Bali, T. Shoji, Accelerated test for evaluation of intergranular stress corrosion cracking initiation characteristics of non-sensitized 316 austenitic stainless steel in simulated pressure water reactor environment, Corros. Sci. 115 (2017) 106—117.

[4] M.B. Toloczko, M.J. Olszta, D.K. Schreiber, S.M. Bruemmer, Corrosion and Stress Corrosion Crack Initiation of Cold-worked Alloy 690 in PWR Primary Water, 2013 downloaded from, https://lwrs.inl.gov/Materials%20Aging%20and%20Degradation/Cold-Worked_Alloy_690_M2LW-13OR0402035.pdf.

[5] M.J. Buehler, J. Dodson, A.C.T. van Duin, P. Meulbroek, W.A. Goddard, The computational materials design facility (CMDF): a powerful framework for multi-paradigm multi-scale simulations, in: Materials Research Society Symposium Proceedings, 2006 downloaded from, http://web.mit.edu/mbuehler/www/research/CMDF/MRS-proc-2006-CMDF.pdf.

[6] M.J. Buehler, T. Ackbarow, Fracture mechanics of protein materials, Mater. Today 10 (2007) 46—58.

[7] S. Keten, M.J. Buehler, Large deformation and fracture mechanics of beta-helical protein nanotube: atomistic and continuum modeling, Comp. Method. Appl. M 197 (2008) 3203–3214.

[8] C. Lorenz, N.L. Doltsinis, Molecule dynamics simulation: from "ab initio" to "coarse grained", in: J. Leszczynski, A. Kaczmarek-Kedziera, T. Puzyn, M.G. Papadopoulos, H. Reis, M.K. Shukla (Eds.), Handbook of Computational Chemistry, Springer International Publishing, 2017, pp. 337–396.

[9] S.J. Zinkle, G.S. Was, Materials challenges in nuclear energy, Acta Mater. 61 (2013) 735–758.

[10] T. Allen, J. Busby, M. Meyer, D. Petti, Materials challenges for nuclear systems, Mater. Today 13 (2010) 14–23.

[11] G.S. Was, P. Ampornrat, G. Gupta, S. Teysseyre, E.A. West, T.R. Allen, K. Sridharan, L. Tan, Y. Chen, X. Ren, C. Pister, Corrosion and stress corrosion cracking in supercritical water, J. Nucl. Mater. 371 (2007) 176–201.

[12] J.H. Liu, G. Bin, The Effect of Dissolved Oxygen on Stress Corrosion Cracking of 310S in SCW, 2016 downloaded from, https://www.iaea.org/NuclearPower/Downloadable/Meetings/2016/2016-10-10-10-14-NPTDS/III-5_J.Liu_The_effect_of_dissolved_oxygen.pdf.

[13] M. Nezakata, H. Akhiania, S. Penttiläb, S.M. Sabetc, J. Szpunara, Effect of thermo-mechanical processing on oxidation of austenitic stainless steel 316L in supercritical water, Corros. Sci. 94 (2015) 197–206.

[14] T. Terachi, K. Fujii, K. Arioka, Microstructural characterization of SCC crack tip and oxide film for SUS 316 stainless steel in simulated PWR primary water at 320°C, J. Nucl. Sci. Technol. 42 (2005) 225–232.

[15] S.E. Ziemniak, M. Hanson, Corrosion behavior of 304 stainless steel in high temperature hydrogenated water, Corros. Sci. 44 (2002) 2209–2230.

[16] S. Lozano-Perez, K. Kruska, I. Iyengarb, T. Terachic, T. Yamadac, The role of cold work and applied stress on surface oxidation of 304 stainless steel, Corros. Sci. 56 (2012) 78–85.

[17] G.S. Was, S. Teysseyre, Z. Jiao, Corrosion of austenitic alloys in supercritical water, Corrosion 63 (2006) 989–1005.

[18] S. Cissé, L. Laffont, B. Tanguy, M.C. Lafont, E. Andrieu, Effect of surface preparation on the corrosion of austenitic stainless steel 304L in high temperature steam and simulated PWR primary water, Corros. Sci. 56 (2012) 209–216.

[19] M. Fulger, M. Mihalache, D. Ohai, S. Fulger, S.C. Valeca, Analyses of oxide films grown on AlSi 304L stainless steel and Incoloy 800HT exposed to supercritical water environment, J. Nucl. Mater. 415 (2011) 147–157.

[20] M.C. Sun, X.Q. Wu, Z.E. Zhang, E.H. Han, Oxidation of 316 stainless steel in supercritical water, Corros. Sci. 51 (2009) 1069–1072.

[21] M. Da Cunha Belo, M. Walls, N.E. Hakiki, J. Coset, E. Picquenard, G. Sagon, D. Noel, Composition, structure and properties of the oxide films formed on the stainless steel 316L in a primary type PWR environment, Corros. Sci. 40 (1998) 447–463.

[22] S.E. Ziemniak, M. Hanson, Corrosion behavior of NiCrFe alloy 600 in high temperature hydrogenated water, Corros. Sci. 48 (2006) 498–521.

[23] Y.L. Han, J.N. Mei, Q.J. Peng, E.H. Han, W. Ke, Effect of electropolishing on corrosion of Alloy 600 in high temperature water, Corros. Sci. 98 (2015) 72–80.

[24] T. Nakagawa, N. Totsuka, T. Terachi, N. Nakajima, Influence of dissolved hydrogen on oxide film and PWSCC of Alloy 600 in PWR primary water, J. Nucl. Sci. Technol. 40 (2003) 39–43.

[25] Y.S. Lim, H.P. Kim, S.S. Hwang, Microstructural characterization on intergranular stress corrosion cracking of Alloy 600 in PWR primary water environment, J. Nucl. Mater. 440 (2013) 46–54.

[26] D. Morton, N. Lewis, M. Hanson, S. Rice, P. Sanders, Nickel Alloy Primary Water Bulk Surface and SCC Corrosion Film Analytical Characterization and SCC Mechanistic Implications (LM-07K022), 2007 downloaded from, http://www.osti.gov/scitech/servlets/purl/903204/.

[27] T. Moss, G.P. Cao, G.S. Was, Oxidation of alloy 600 and alloy 690: experimentally accelerated study in hydrogenated supercritical water, Metall. Mat. Trans. A 48 (2017) 1596–1612.

[28] S.E. Ziemniak, M. Hanson, Corrosion behavior of NiCrMo alloy 625 in high temperature, hydrogenated water, Corros. Sci. 45 (2003) 1595–1618.

[29] M.C. Sun, X.Q. Wu, Z.E. Zhang, E.H. Han, Analysis of oxide film grown on Alloy 625 in oxidizing supercritical water, J. Supercrit. Fluid 47 (2008) 309–317.

[30] K.H. Chang, J.S. Huang, C.B. Yan, T.K. Yeh, F.R. Chen, J.J. Kai, Corrosion behavior of Alloy 625 in supercritical water environments, Prog. Nucl. Energy 57 (2012) 20–31.

[31] W.J. Kuang, X.Q. Wu, E.H. Han, J.C. Rao, The mechanism of oxide film formation on alloy 690 in oxygenated high temperature water, Corros. Sci. 53 (2011) 3853–3860.

[32] M. Sennour, L. Marchetti, F. Martin, S. Perri, R. Molins, M. Pijolat, A detailed TEM and SEM study of Ni-base alloys oxide scales formed in primary conditions of pressurized water reactor, J. Nucl. Mater. 402 (2010) 147–156.

[33] X.Y. Zhong, E.H. Han, X.Q. Wu, Corrosion behavior of Alloy 690 in aerated supercritical water, Corros. Sci. 66 (2013) 369–379.

[34] F. Huang, J.Q. Wang, E.H. Han, W. Ke, Microstructural characteristics of the oxide films formed on Alloy 690 TT in pure and primary water at 325°C, Corros. Sci. 76 (2013) 52–59.

[35] C. Maffiotte, A.S. Maderuelo, D.G. Briceño, AES characterization of oxide films formed on nickel-base alloys at supercritical water reactor (SCWR) conditions, Surf. Interface Anal. (2015), https://doi.org/10.1002/sia.5906.

[36] S. Bruemmer, M. Olszta, D. Schreiber, M. Toloczko, SCC initiation measurements on alloy 600 and 690 materials in PWR primary water, in: Alloy 690/52/152 PWSCC Research Collaboration Meeting (Conference Presentation), Electric Power Research Institute, Tampa, Florida, USA, 2014.

[37] J. Panter, B. Viguier, J.M. Cloué, M. Foucault, P. Combrade, E. Andrieu, Influence of oxide films on primary water stress corrosion cracking initiation of alloy 600, J. Nucl. Mater. 348 (2006) 213–221.

[38] W.W. Wang, Z.L. Zhang, X.C. Ren, Y.J. Guan, Y.J. Su, Corrosion product film-induced stress facilitates stress corrosion cracking, Sci. Rep. (2015), https://doi.org/10.1038/srep10579.

[39] K. Kruska, S.L. Perez, D.W. Saxey, T. Terachi, T. Yamada, G.D.W. Smith, Nanoscale characterisation of grain boundary oxidation in cold-worked stainless steels, Corros. Sci. 63 (2012) 225–233.

[40] S. Lozano-Perez, A guide on FIB preparation of samples containing stress corrosion crack tips for TEM and atom-probe analysis, Micron 39 (2008) 320–328.

[41] S. Lozano-Perez, T. Yamada, T. Terachi, M. Schröder, C.A. English, G.D.M. Smith, C.R.M. Grovenor, B.L. Eyre, Multi-scale characterization of stress corrosion cracking of cold-worked stainless steels and the influence of Cr content, Acta Mater. 57 (2009) 5361–5381.

[42] S. Lozano-Perez, P. Rodrigo, L.C. Gontard, Three-dimensional characterization of stress corrosion cracks, J. Nucl. Mater. 408 (2011) 289–295.

[43] Y.H. Lu, Q.J. Peng, T. Sato, T. Shoji, An ATEM study of oxidation behavior of SCC crack tips in 304L stainless steel in high temperature oxygenated water, J. Nucl. Mater. 347 (2005) 52–68.

[44] S.M. Bruemmer, L.E. Thomas, High-resolution characterizations of stress-corrosion cracks in austenitic stainless steel from crack growth tests in BWR-simulated environments, in: Proceedings of the 12th International Conference on Environmental Degradation of Materials in Nuclear Power System-water Reactors, 2005, pp. 189–197 downloaded from, http://iweb.tms.org/NM/NM-0702-5.pdf.

[45] M. Meisnar, M. Moody, S.L. Perez, Atom probe tomography of stress corrosion crack tips in SUS316 stainless steels, Corros. Sci. 98 (2015) 661–671.

[46] M. Meisnar, A. Vilalta-Clemente, A. Gholinia, M. Moody, A.J. Wilkinson, N. Huin, S. Lozano-Perez, Using transmission Kikuchi diffraction to study intergranular stress corrosion cracking in type 316 stainless steels, Micron 75 (2015) 1–10.

[47] S.M. Bruemmer, L.E. Thomas, High-resolution Analytical Electron Microscopy Characterization of Stress Corrosion Crack Tips, 2001 (ICF100890OR), downloaded from, http://www.gruppofrattura.it/ocs/index.php/ICF/ICF10/paper/view/4752/6759.

[48] H.P. Kim, D.J. Kim, S.W. Kim, Y.S. Lim, S.S. Hwang, Ex situ and in situ characterization of stress corrosion cracking of nickel-base alloys at high temperature, J. Solid State Electr 18 (2014) 309–323.

[49] C. Guerre, Stress corrosion cracking of nickel base alloys in PWR primary water, A report in the MINOS Workshop, Materials Innovation for Nuclear Optimized Systems Workshop, December 5–7, 2012, CEA-INSTN Saclay, France, http://dx.doi.org/10.105.1/epjconf/20135104003.

[50] J. Lindsay, Stress Corrosion Cracking and Internal Oxidation of Alloy 600 in High Temperature Hydrogenated Steam and Water, Ph.D. thesis, University of Manchester, 2014.

[51] Y.S. Lim, S.W. Kim, S.S. Hwang, H.P. Kim, C.H. Jang, Intergranular oxidation of Ni-based Alloy 600 in a simulated PWR primary water environment, Corros. Sci. 108 (2016) 125–133.

[52] M. Sennour, P. Laghoutaris, C. Guerre, R. Molins, Advanced TEM characterization of stress corrosion cracking of Alloy 600 in pressurized water reactor primary water environment, J. Nucl. Mater. 393 (2009) 254–266.

[53] D.K. Schreiber, M.J. Olszta, D.W. Saxey, K. Kruska, K.L. Moore, S.L. Perez, S.M. Bruemmer, Examinations of oxidation and sulfidation of grain boundaries in alloy 600 exposed to simulated pressurized water reactor primary water, Microsc. Microanal 19 (2013) 676–687.

[54] S.Y. Persaud, A. Korinek, J. Huang, G.A. Botton, R.C. Newman, Internal oxidation of Alloy 600 exposed to hydrogenated steam and the beneficial effects of thermal treatment, Corros. Sci. 86 (2014) 108–122.

[55] G. Bertail, F. Scenini, M.G. Burke, The intergranular oxidation susceptibility of thermally-treated Alloy 600, Corros. Sci. 114 (2017) 112–122.

[56] K. Arioka, R.W. Staehle, T. Yamada, T. Miyamoyo, T. Terachi, Degradation of Alloy 690 after relatively short times, Corrosion 72 (2016) 1252–1268.

[57] H. Dugdale, D.E.J. Armstrong, E. Tarleton, S.G. Roberts, S. Lozano-Perez, How oxidized grain boundaries fail, Acta Mater. 61 (2013) 4707–4713.

[58] O. Verners, A.C.T. Van Duin, Comparative molecular dynamics study of fcc-Ni nanoplate stress corrosion in water, Surf. Sci. 633 (2015) 94–101.

[59] M.L. Rossi, C.D. Taylor, A.C.T. van Duin, Reduced yield stress for zirconium exposed to iodine: reactive force field simulation, Adv. Model. Simulation Eng. Sci. 2 (2014) 19–27, https://doi.org/10.1186/s40323-014-0019-z.

[60] C.L. White, Grain Boundary Segregation and Intergranular Failure. International Al-Li Conference, 19 May 1980. Stone Mountain, Ga.

[61] M. Yamaguchi, M. Shiga, H. Kaburaki, Grain boundary decohesion by sulfur segregation in ferromagnetic iron and nickel-a first-principles study, Mater. Trans. 47 (2006) 2682–2689.

[62] H.P. Chen, R.K. Kalia, E. Kaxiras, G. Lu, A. Nakano, K.I. Nomura, A.C.T. van Duin, P. Vashishta, Z. Yuan, Embrittlement of metal by solute segregation-induced amorphization, Phys. Rev. Lett. 104 (2010) 155502 (1-4).

[63] K. Kruska, Understanding the Mechanism of Stress Corrosion Cracking, Ph.D. thesis, University of Oxford, 2012.

[64] P.M. Scott, M. Le Calvar, The Proceedings of the Sixth International Symposium on Environmental Degradation of Materials in Nuclear Power Systems—water Reactors, 1993, pp. 657—665.

[65] A. Stratulat, D.E.J. Armstrong, S.G. Roberts, Micro-mechanical measurement of fracture behaviour of individual grain boundaries in Ni alloy 600 exposed to a pressurized water reactor environment, Corros. Sci. 104 (2016) 9—16.

[66] B. Langelier, S.Y. Persaud, A. Korinek, T. Casagrande, R.C. Newman, G.A. Botton, Effects of boundary migration and pinning particles on intergranular oxidation revealed by 2D and 3D analytical electron microscopy, Acta Mater. 131 (2017) 280—295.

[67] D.K. Schreiber, S.M. Bruemmer, M.J. Olszta, Grain boundary depletion and migration during selective oxidation of Cr in a Ni-5Cr binary alloy exposed to high-temperature hydrogenated water, Scripta Mater. 89 (2014) 41—44.

[68] R.W. Balluffi, Grain boundary diffusion mechanisms in metals, J. Electron. Mater. 21 (1992) 527—553.

[69] D. Raabe, M. Herbig, S. Sandlöbes, Y. Li, D. Tytko, M. Kuzmina, D. Ponge, P.P. Choi, Grain boundary segregation engineering in metallic alloys: a pathway to the design of interfaces, Curr. Opin. Solid St. M. S. 18 (2014) 253—261.

[70] J.W. Cahn, Diffusion induced grain boundary migration, Scripta Metall. 13 (1979) 503—509.

[71] R.W. Balluffi, J.W. Cahn, Mechanism for diffusion induced grain boundary migration, Acta Metall. 29 (1981) 493—500.

[72] R.W. Balluffi, T. Kwok, P.D. Bristowe, A. Brokman, P.S. Ho, S. Yip, Determination of vacancy mechanism for grain boundary self-diffusion by computer simulation, Scripta Metall. 15 (1981) 951—956.

[73] M. Olszta, D. Schreiber, L. Thomas, S. Bruemmer, High-resolution crack imaging reveals degradation processes in nuclear reactor structural materials, Adv. Mater. Process. 170 (2012) 17—21.

[74] C.C.F. Amaral, F. Ormiga, J.A.C.P. Gomes, Electrochemical-induced dissolution of stainless steel files, Int. Endod. J. 48 (2015) 137—144.

[75] J.M. Wang, H. Lu, L.F. Zhang, F.J. Meng, X.L. Xu, Effects of dissolved gas and cold work on the electrochemical behaviors of 304 stainless steel in simulated PWR primary water, Corrosion 73 (2017) 281—289.

[76] Y.J. Kim, P.L. Andresen, Data quality, issues and guidelines for electrochemical corrosion potentials measurement in high-temperature water, Corrosion 59 (2003) 584—596.

[77] Y. Behnamian, A. Mostafaei, A. Kohandehghan, B. Zahiri, W.Y. Zheng, D. Guzonas, M. Chmielus, W.X. Chen, J.L. Luo, Corrosion behavior of alloy 316L stainless steel after exposure to supercritical water at 500°C for 20,000 h, J. Supercrit. Fluids 127 (2017) 191—199.

[78] D. Sengupta, S. Kwak, A. Vasenkov, Y.K. Shin, A.C.T. van Duin, reportComputational Capabilities for Predictions of Interactions at the Grain Boundary of Refractory Alloys. Project Report, downloaded from: https://www.osti.gov/scitech/biblio/1170170.

[79] J. Robertson, The mechanism of high temperature aqueous corrosion of stainless steels, Corros. Sci. 32 (1991) 443—465.

[80] B. Stellwag, The mechanism of oxide film formation on austenitic stainless steels in high temperature water, Corros. Sci. 40 (1998) 337—370.

[81] C.Y. Zou, Y.K. Shin, A.C.T. van Duin, H.Z. Fang, Z.K. Liu, Molecular dynamics simulations of the effects of vacancies on nickel self-diffusion, oxygen diffusion and oxidation initiation in nickel, using the ReaxFF reactive force field, Acta Materialia 83 (2015) 102—112.

[82] Lide DR. Handbook of chemistry and physics.

[83] D.A. Newsome, D. Sengupta, A.C.T. van Duin, High-temperature oxidation of SiC-based composite: rate constant calculation from ReaxFF MD simulation, part II, J. Phys. Chem. C 117 (2013) 5014—5027.

[84] L. Marchetti, S. Perrin, F. Jambon, M. Pijolat, Corrosion of nickel-base alloys in primary medium of pressurized water reactors: new insights on the oxide growth mechanisms and kinetic modeling, Corros. Sci. 102 (2016) 24—35.

[85] M. Dumerval, S. Perrin, L. Marchetti, M. Sennour, F. Jomard, S. Vaubaillon, Y. Wouters, Effect of implantation defects on the corrosion of 316L stainless steels in primary medium of pressurized water reactors, Corros. Sci. 107 (2016) 1—8.

[86] V. Alexandrov, M.L. Sushko, D.K. Schreiber, S.M. Bruemmer, K.M. Rosso, Ab initio modeling of bulk and intragranular diffusion in Ni alloys, J. Phys. Chem. Lett. 6 (2015) 1618—1623.

[87] A. Paul, T. Laurila, V. Vuorinen, S.V. Divinski, Thermodynamics, Diffusion and the Kirkendall Effect in Solids, Springer Cham Heidelberg, New York Dordrecht London, 2014.

[88] Y. Yang, K.G. Field, T.R. Allen, J.T. Busby, Roles of vacancy/interstitial diffusion and segregation in the microchemistry at grain boundaries of irradiated Fe-Cr-Ni alloys, J. Nucl. Mater. 473 (2016) 35—53.

[89] D. Farkas, Atomistic theory and computer simulation of grain boundary structure and diffusion, J. Phys. Condens. Matter 12 (2000) R497—R516.

[90] G.R. Love, Dislocation pipe diffusion, Acta Metall. 12 (1964) 731—737.

[91] M. Legros, G. Dehm, E. Arzt, J.B. John, Observation of giant diffusivity along dislocation cores, Science 21 (2008) 1646—1649.

[92] C.O.T. Galvin, M.W.D. Cooper, P.C.M. Fossati, C.R. Stanek, R.W. Grimes, D.A. Andersson, Pipe and grain boundary diffusion of He in UO2, J. Phys. Condens. Matter 28 (2016) 405002 (1-11).

[93] Y. Mishin, Chr Herzig, J. Bernardini, W. Gust, Grain boundary diffusion: fundamentals to recent developments, Int. Mater. Rev. 42 (1997) 155—178.

[94] S. Sarrade, D. Féron, F. Rouillard, S. Perrin, S. Robin, J.C. Ruiz, H.A. Turc, Overview on corrosion in supercritical fluids, J. Supercrit. Fluids 120 (2017) 335—344.

[95] R.W. Balluffi, On measurements of self-diffusion rates along dislocations in F.C.C. metals, Phys. Stat. Sol 42 (1970) 11—34.

[96] N.L. Peterson, Grain-boundary diffusion in metals, Int. Meter. Rev. 28 (1983) 65—91.

[97] Y. Mishin, C. Herzig, J. Bernardini, W. Gust, Grain boundary diffusion: fundamentals to recent developments, Int. Mater. Rev. 42 (1997) 155—178.

[98] A.H. King, Diffusion induced grain boundary migration, Int. Mater. Rev. 32 (1987) 173—189.

[99] A. Azizi, X.L. Zou, P. Ercius, Z.H. Zhang, A.L. Elías, N. Perea-Lopez, G. Stone, M. Terrones, B.I. Yakobson, N. Alem, Dislocation motion and grain boundary migration in two-dimensional tungsten disulphide, Nat. Commun. 4867 (2014) 1—7.

[100] K.G.F. Janssens, D. Olmsted, E.A. Holm, S.M. Foiles, S.L. Plimpton, P.M. Derlet, Computing the mobility of grain boundaries, Nat. Mater. 5 (2006) 124—127.

[101] M.J. Buehler, A. Hartmaier, M.A. Duchaineau, F.F. Abraham, H.J. Gao, The dynamical complexity of work-hardening: a large-scale molecular dynamics simulation, Acta Mech. Sinica 21 (2005) 103—111.

[102] C. Thaulow, D. Sen, M.J. Buehler, Atomistic study of the effect of crack tip ledges on the nucleation of disloations in silicon single crystals at elevated temperature, Mat. Sci. Eng. A 528 (2011) 4357—4364.

[103] R.O. Ritchie, Failure of silicon: crack formation and propagation, in: 13th Workshop on Crystalline Solar Cell Materials and Processes, August 2003. Vail, Colorado, USA. Downloaded from, http://robotics.eecs.berkeley.edu/~pister/147/SiliconFailureRitchie2003.pdf.

[104] G. Bertali, F. Scenini, M.G. Burke, The effect of residual stress on the preferential intergranular oxidation of Alloy 600, Corros. Sci. 111 (2016) 494—507.

[105] P.J. Withers, Fracture mechanics by three-dimensional crack-tip synchrotron X-ray microscopy, Phil. Trans. R. Soc. A 373 (2015) 20130157, https://doi.org/10.1098/rsta.2013.0157.

[106] M.J. Buehler, Z.P. Xu, Mind the helical crack, Nature 464 (2010) 42—43.

[107] E. Bitzek, J.R. Kermode, P. Gumbsch, Atomistic aspects of fracture, Int. J. Fract 191 (2015) 13—30.

[108] A. Gleizer, G. Peralta, J.R. Kermode, A. De Vita, D. Sherman, Dissociative Chemisorption of O2 inducing stress corrosion cracking in silicon crystals, Phys. Rev. Lett. 112 (2014) 115501 (1-5).

[109] K. Nomura, Y.C. Chen, W.Q. Wang, R.K. Kalia, A. Nakano, P. Vashishta, L.H. Yang, Interaction and coalescence of nanovoids and dynamic fracture in silica glass: multimillion-to-billion atom molecular dynamics simulations, J. Phys. D. Appl. Phys. 42 (2009) 214011 (1-12).

[110] A. King, G. Johnson, D. Engelberg, W. Ludwig, J. Marrow, Observations of intergranular stress corrosion cracking in a grain-mapped polycrystal, Science 321 (2008) 382—385.

[111] M.J. Buehler, H.J. Gao, Dynamical fracture instabilities due to local hyperelasticity at crack tips, Nature 439 (2006) 307—310.

[112] V. Priya, K.K. Rajiv, N. Aiichiro, K. Efthimios, G. Ananth, L. Gang, E. Stephan, V.F. Arthur, H.Q. Rnady, M.A. John, Y.H. Lin, Hierarchical Petascale Simulation Framework for Stress Corrosion Cracking. Project Report of Scientific Discovery Through Advanced Computing (Grant Number: DE-FC02-06ER25788), 2014 downloaded from, https://www.osti.gov/scitech/servlets/purl/1164641.

[113] O. Verners, Molecular Dynamics Analysis of Oxidation, Segregation and Stress Corrosion Failure of Refractory Alloys, Ph.D. thesis, The Pennsylvania State University, 2014.

[114] T.T. Nguyen, J. Bolivar, J. Réthoré, M.C. Baietto, M. Fregonese, A phase field method for modeling stress corrosion crack propagation in a nickel base alloy, Int. J. Solids Struct. 112 (2017) 65—82.

[115] M.J. Buehler, F.F. Abraham, H.J. Gao, Hyperelasticity governs dynamic fracture at a critical length scale, Nature 426 (2003) 141—146.

[116] W.G. Hwang, S.G. Bae, J.S. Kim, B.Y. Lee, Acoustic emission characteristics of stress corrosion cracks in a type 304 stainless steel tube, Nucl. Eng. Technol. 47 (2015) 454—460.

[117] J.S. Kim, B.Y. Lee, W.G. Hwang, S.S. Kang, The effect of welding residual stress for making artificial stress corrosion crack in the STS 304 pipe, Adv. Mater. Sci. Eng. 2015 (2015) 7, https://doi.org/10.1155/2015/932512. Article ID 932512.

[118] P. Andresen, SCC of Alloys 152/52/52i Weld Metal in PWR Water (Conference Presentation), Alloy 690/52/152 PWSCC Research Collaboration Meeting, Electric Power Research Institute, Tampa, Florida, USA, December 2-4, 2014.

[119] M. Morra, M. Othon, S. McCracken, B. Sutton, A. Ahluwalia, Analysis Narrow Groove 52M Welds SA508 and SA508 to Alloy 690 (Conference Presentation), Alloy 690/52/152 PWSCC Research Collaboration Meeting, Electric Power Research Institute, Tampa, Florida, USA, December 2-4, 2014.

[120] S. Bruemmer, M.J. Olszta, N.R. Overman, M.B. Toloczko, Cold-work effects on stress corrosion crack growth in Alloy 690 tubing and plate materials, in: 17th International Conference on Environmental Degradation of Materials in Nuclear Power System-water Reactors, Ottawa, Ontario, Canada, August 9-12, 2015.

[121] S. Bruemmer, M.J. Olszta, N. Overman, M. Toloczko, Cold and warm work effects on stress corrosion crack growth in Alloy 690 materials (conference presentation), in: ICG-EAC Meeting, Ann Arbor, Michigan, USA, May 18-22,

2015 downloaded from, https://www.nrc.gov/docs/ML1514/ML15140A420.pdf.

[122] W.Q. Zhang, K.W. Fang, Y.J. Hu, S.Y. Wang, X.L. Wang, Effect of maching-induced surface residual stress on initiation of stress corrosion cracking in 316 austenitic stainless steel, Corros. Sci. 108 (2016) 173—184.

[123] S.M. Bruemmer, M.J. Olszta, N.R. Overman, M.B. Toloczko, Microstructural effects on stress corrosion crack growth in cold-worked alloy 690 tubing and plate materials, in: 16th International Conference on Environmental Degradation of Materials in Nuclear Power Systems-water Reactors, Asheville, North Carolina, USA, 2013 downloaded from, https://www.nrc.gov/docs/ML1322/ML13220A048.pdf.

[124] S.M. Bruemmer, M.J. Olszta, M.B. Toloczko, L.E. Thomas, Linking microstructure to stress corrosion cracking of cold rolled alloy 690 in PWR primary water, Corrosion 69 (2013) 953—963.

[125] J. Hou, Q.J. Peng, Z.P. Lu, T. Shoji, J.Q. Wang, E.H. Han, W. Ke, Effects of cold working degrees on grain boundary characters and strain concentration at grain boundaries in Alloy 600, Corros. Sci. 53 (2011) 1137—1142.

[126] D. Groen, S.J. Zasada, P.V. Coveney, Survey of multiscale and multiphysics applications and communities, Comput. Sci. Eng. 16 (2013) 34—43.

[127] S.J. Plimpton, A.P. Thompson, Computational aspects of many-body potentials, MRS Bull. 37 (2012) 513—521.

[128] M.L. Sushko, V. Alexandrov, D.K. Schreiber, K.M. Rosso, S.M. Bruemmer, Multiscale model of metal alloy oxidation at grain boundaries, J. Chem. Phys. 142 (2015), 214114-1—214114-8.

[129] R.A. Friesner, Ab initio quantum chemistry: methodology and applications, P. Natl. Acad. Sci. USA 102 (2005) 6648—6653.

[130] J.T. Hynes, Molecules in motion: chemical reaction and allied dynamics in solution and elsewhere, Annu. Rev. Phys. Chem. 66 (2015) 1—20.

[131] K. Kang, Y.S. Meng, J. Bréger, C.P. Grey, G. Ceder, Electrodes with high power and high capacity for rechargeable lithium batteries, Science 311 (2006) 977—980.

[132] L. Kunz, F.M. Kuhn, O. Deutschmann, Kinetic Monte Carlo simulations of surface reactions on supported nanoparticles: a novel approach and computer code, J. Chem. Phys. 143 (2015), 044108-1-10.

[133] I.B. Obot, D.D. Macdonald, Z.M. Gasem, Density functional theory (DFT) as a powerful tool for designing new organic corrosion inhibitors Part 1: an overview, Corros. Sci. 99 (2015) 1—30.

[134] M. Pavone, A.B. Muñoz-García, A.M. Ritzmann, E.A. Carter, First-principles study of lanthanum strontium manganite: insights into electronic structure and oxygen vacancy formation, J. Phys. Chem. C 118 (2014) 13346—13356.

[135] T. Tan, X.L. Yang, C.M. Krauter, Y.G. Ju, E.A. Carter, Ab initio kinetics of hydrogen abstraction from methyl acetate by hydrogen, methyl, oxygen, hydroxyl, and hydroperoxy radicals, J. Phys. Chem. A 119 (2015) 6277—6390.

[136] R.E. Thomas, G.H. Booth, A. Alavi, Accurate ab initio calculation of ionization potentials of the first-row transition metals with the configuration-interaction quantum Monte Carlo technique, Phys. Rev. Lett. 114 (2015) 033001, https://doi.org/10.1103/PhysRevLett.114.033001.

[137] A.C.T. van Duin, S. Dasgupta, F. Lorant, W.A. Goddard, ReaxFF: a reactive force field for hydrocarbons, J. Phys. Chem. A 105 (2001) 9396—9409.

[138] T.P. Senftle, S.H. Md Mahbubul Islam, S.B. Kylasa, Y.X. Zheng, Y.K. Shin, C. Junkermeier, R. Engel-Herbert, M.J. Janik, H.M. Aktulga, T. Verstraelen, A. Grama, A.C.T. van Duin, The ReaxFF reactive force-field: development, applications and future directions, npj Computational Mater. 2 (2016), 15011, https://doi.org/10.1038/npjcompumats.2015.11.

[139] T.R. Shan, B.D. Devine, T.W. Kemper, S.B. Sinnott, S.R. Phillpot, Charged-optimized many-body potential for the hafnium/hafnium oxide system, Phys. Rev. B 81 (2010) 125328.

[140] X.W. Zhou, F.P. Doty, Embedded-ion method: an analytical energy-conserving charge-transfer interatomic potential and its application to the La-Br system, Phys. Rev. B 78 (2008) 224307.

[141] D.W. Brenner, O.A. Shenderova, J.A. Harrison, S.J. Stuart, B. Ni, S.B. Sinnott, A second-generation reactive empirical bond order (REBO) potential energy expression for hydrocarbons, J. Phys. Condens. Matter 14 (2002) 783—802.

[142] S.J. Stuart, A.B. Tutein, J.A. Harrison, A reactive potential for hydrocarbons with intermolecular interactions, J. Chem. Phys. 112 (2000) 6472—6486.

[143] F.H. Streitz, J.W. Mintmire, Electrostatic potentials for metal-oxide surfaces and interfaces, Phys. Rev. B 50 (1994) 11996—12003.

[144] J. Tersoff, New empirical approach for the structure and energy of covalent systems, Phys. Rev. B 37 (1988) 6991—7000.

[145] M.J. Buehler, A.C.T. van Duin, W.A. Goddard, Multiparadigm modeling of dynamical crack propagation in silicon using a reactive force field, Phys. Rev. Lett. 96 (2006), 095505-1-095505-4.

[146] M.M. Islam, C.Y. Zou, A.C.T. van Duin, S. Raman, Interactions of hydrogen with the iron and iron carbide interfaces: a ReaxFF molecular dynamics study, Phys. Chem. Chem. Phys. 2 (2016) 761—771.

[147] M.L. Rossi, C.D. Taylor, First-principles insights into the nature of zirconium-iodine interactions and the initiation of iodine-induced stress corrosion cracking, J. Nucl. Mater. 458 (2015) 1—10.

[148] G.J. Tainter, G.C. Schatz, Reactive force field modeling of zinc oxide nano-particle formation, J. Phys. Chem. C 120 (2016) 2950—2961.

[149] W. Barrows, R. Dingreville, D. Spearot, Traction—separation relationships for hydrogen induced grain boundary embrittlement in nickel via molecular dynamics simulations, Mat. Sci. Eng. A 650 (2016) 354—364.

[150] X.Y. Li, H.J. Gao, Atomistic modeling of deformation and failure mechanisms in nanostructured materials, Natl. Sci. Rev. 2 (2015) 133—136.

[151] D.R. Alfonso, D.N. Tafen, Simulation of atomic diffusion in the Fcc NiAl system: a kinetic Monte Carlo study, J. Phys. Chem. C 119 (2015) 11809—11817.

[152] M. Ma, G. Tocci, A. Michaelides, G. Aeppli, Fast diffusion of water nano-droplets on graphene, Nat. Mater. 15 (2016) 66—71.

[153] M.I. Mendelev, C. Deng, C.A. Schuh, D.J. Srolovitz, Comparison of molecular dynamics simulation methods for the study of grain boundary migration, Model. Simul. Mater. Sci. Eng 21 (2013), https://doi.org/10.1088/0965-0393/21/4/045017.

[154] I.I. Novoselov, A.V. Yanilkin, Impact of segregated interstitials on structures and energies of tilt grain boundaries in Mo, Comp. Mater. Sci. 112 (2016) 276—281.

[155] O. Senninger, F. Soisson, E. Martínez, M.C. Fu, Y. Bréchet, Modeling radiation induced segregation in iron—chromium alloys, Acta Materialia 103 (2016) 1—11.

[156] Y. Sun, S. Hara, Atomistic study of segregation and diffusion of yttrium and calcium cations near electrolyte surfaces in solid oxide fuel cells, J. Eur. Ceram. Soc. 35 (2015) 3063—3074.

[157] F. Ulomek, V. Mohles, Separating grain boundary migration mechanisms in molecular dynamics simulation, Acta Mater. 103 (2016) 424—432.

[158] M. Upmanyu, D.J. Srolovitz, A.E. Lobkovsky, J.A. Warren, W.C. Carter, Simultaneous grain boundary migration and grain rotation, Acta Mater. 54 (2006) 1707—1719.

[159] J. Hemminger, G. Crabtree, J. Sarrao, From quanta to the continuum: opportunity for mesoscale science. A Report for the Basic Energy Sciences Advisory Committee Mesoscale Science Subcommittee, 2012. http://science.energy.gov/~/media/bes/pdf/reports/files/OFMS_rpt.pdf.

[160] J.S. Chen, H.S. Lu, D. Moldovan, D. Wolf, Mesoscale modeling of grain boundary migration under stress using coupled finite element and meshfree methods, 15th ASCE Engineering Mechanics Conference, Columbia University, New York, NY (US), 06/02/2002—06/05/2002. downloaded from: https://searchworks.stanford.edu/view/11318775.

[161] C.P. Race, R. Hadian, J. von Pezold, B. Grabowski, J. Neugebauer, Mechanisms and kinetics of the migration of grain boundaries containing extended defects, Phys. Rev. B 92 (2015) 174115, https://doi.org/10.1103/PhysRevB.92.174115.

[162] C.P. Race, J. von Pezold, J. Neugebauer, Role of the mesoscale in migration kinetics of flat grain boundaries, Phys. Rev. B 89 (2014) 214110.

[163] Q. Du, R. Lipton, Peridynamics, fracture, and nonlocal continuum models, SIAM News 47 (2014) downloaded from, https://www.siam.org/pdf/news/2148.pdf.

[164] A.D. Rollett, G.S. Rohrer, R.M. Suter, Understanding materials microstructure and behavior at the mesoscale, MRS Bull. 40 (2015) 951—958.

[165] A.P. Jivkov, N.P.C. Stevens, T.J. Marrow, A two-dimensional mesoscale model for intergranular stress corrosion crack propagation, Acta Mater. 54 (2006) 3493—3501.

[166] T.L. Xu, R. Stewart, J.H. Fan, X.G. Zeng, A.L. Yao, Bridging crack propagation at the atomistic and mesoscopic scale for BCC-Fe with hybrid multiscale methods, Eng. Fract. Mech. 155 (2016) 166—182.

[167] S. Yip, M.P. Short, Multiscale materials modelling at the mesoscale, Nat. Mater. Commentary 12 (2013) 774—777.

[168] S.A. Silling, Peridynamic Model for Fatigue Cracking, 2014 downloaded from: http://prod.sandia.gov/techlib/access-control.cgi/2014/1418590.pdf.

[169] K. Fu, L. Chang, L. Ye, Y.B. Yin, Indentation stress-based models to predict fracture properties of brittle thin film on a ductile substrate, Surf. Coat. Tech. 296 (2016) 46—57.

[170] H. Haftbaradaran, X.C. Xiao, H.J. Gao, Critical film thickness for fracture in thin-film electrodes on substrates in the presence of interfacial sliding, Modelling Simul, Mater. Sci. Eng. 21 (2013) 074008.